Development of the trigger menu and search for new phenomena in the dilepton final state with the ATLAS detector at the LHC

Tetiana Berger-Hrynova

LAPP-H-2016-002

Université Grenoble Alpes

Mémoire présenté par

Tetiana Berger-Hryn'ova

pour obtenir le diplôme de

Habilitation à Diriger des Recherches

Spécialité: Physique des Particules

Development of the trigger menu and search for new phenomena in the dilepton final state with the ATLAS detector at the LHC

Soutenu le 03/06/2016 devant le jury composé de :

Dr. Stéphane Jézéquel	(LAPP, Annecy-le-Vieux)	Examinateur
Dr. Giovanni Lamanna	(LAPP, Annecy-le-Vieux)	President du Jury
Dr. Fabienne Ledroit-Guillon	(LPSC, Grenoble)	Rapporteuse
Dr. Emmanuel Perez	(CERN, Genève)	Examinateur
Prof. David Strom	(University of Oregon, Eugene)	Rapporteur
Dr. Patrice Verdier	(IN2P3, Paris)	Rapporteur

LAPP-H-2016-002

Université Grenoble Alpes

Mémoire présenté par

Tetiana Berger-Hryn'ova

pour obtenir le diplôme de

Habilitation à Diriger des Recherches

Spécialité: Physique des Particules

Development of the trigger menu and search for new phenomena in the dilepton final state with the ATLAS detector at the LHC

Soutenu le 03/06/2016 devant le jury composé de :

Dr. Stéphane Jézéquel	(LAPP, Annecy-le-Vieux)	Examinateur
Dr. Giovanni Lamanna	(LAPP, Annecy-le-Vieux)	President du Jury
Dr. Fabienne Ledroit-Guillon	(LPSC, Grenoble)	Rapporteuse
Dr. Emmanuel Perez	(CERN, Genève)	Examinateur
Prof. David Strom	(University of Oregon, Eugene)	Rapporteur
Dr. Patrice Verdier	(IN2P3, Paris)	Rapporteur

Contents

Chapter 1

Introduction

Elementary particle physics has made remarkable progress in its hundred years of existence. In the Standard Model of particle physics (SM) we have a comprehensive gauge theory of particle interactions which provides accurate predictions for almost all phenomena in high-energy physics. Its current formulation was finalized in the late 1970s - early 1980s with experimental confirmation of the existence of quarks [1, 2] and $W^{\pm}$ and Z^0 bosons [3, 4, 5, 6]. Since then, the discoveries of the top quark in 1995 [7, 8], the tau neutrino in 2000 [9], and more recently the Higgs boson in 2012 [10, 11] have given further credibility to the SM. The fundamental parameters of the SM can be fitted to all the relevant measurements and this global *electro-weak fit* confirms that all the observations are consistent as shown in Figure 1.1.

Despite of its successes, the SM has some shortcomings. It does not contain any viable dark matter candidate that possesses all the properties required by observational cosmology and also fails to explain the matter/anti-matter asymmetry of the universe. It also does not incorporate neutrino oscillations or account for the accelerating expansion of the universe.

Also the SM has 19 arbitrary parameters (or 26 if we include neutrino masses and mixing). The SM fermion mass parameters span five-six orders of magnitude and the reason for those differences is not understood. Also the Higgs boson mass is at the electro-weak scale ($\sim$125 GeV). This mass is subject to radiative corrections of order $\Delta m_H^2 \propto \Lambda^2$ from quantum loop interactions with fermions and bosons, where Λ is a the cut-off scale of the theory. If the SM is valid up to the Planck scale (Λ_{Pl}), the Higgs mass would be subject to gigantic corrections and the bare Higgs mass would have to be $\mathcal{O}(\Lambda_{Pl})$. The SM would have to be fine-tuned such that quadratic terms of this order cancel to within 100 GeV, which spoils the naturalness of the theory. This fine-tuning would not be necessary if there is new physics at the electro-weak scale.

All the above hints that the SM is an effective theory, a low energy approximation valid up to $\Lambda \approx 1$ TeV, of this complete theory, so-called "Theory of Everything". The nature of this theory is completely unknown, putting us in a unique situation which we have not had for over 50 years now, where we are searching blindly, without any guidance from the theory. Only data can provide us answers to our questions and hopefully bring positive surprises. We are fortunate to possess the tools needed to collect this data, with the Large Hadron Collider (LHC) at the European Organization for Nuclear Research (CERN) and its experiments.

The LHC was proposed in early 1990s with the aim "to produce, not only high energy but a higher luminosity... than existing or planned hadron colliders" [13]. The main constraints on the LHC configuration were brought by the existing tunnel of the Large-Electron-Positron collider (LEP), which fixed the LHC dimensions, and the use of the existing injector complex. The

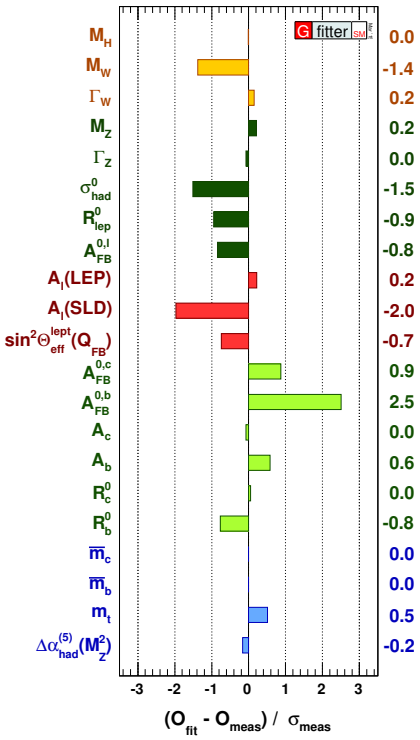

Figure 1.1: Comparing fit results with direct measurements: pull values for the SM fit, i.e. deviations between experimental measurements and theoretical calculations in units of the experimental uncertainty from Ref.[12].

choice to operate it as proton-proton machine[1] allowed it to reach multi-TeV energies without unreasonable operation costs.

Four large experiments (ATLAS, CMS, ALICE and LHCb) are located at the four LHC interaction points. Among these, ATLAS and CMS are general-purpose experiments. The LHCb experiment is more specifically designed to perform precision measurements related to the CP violation and flavor physics studies. Finally, ALICE is dedicated to the exploration of the physical properties of matter under the strong interaction by studying the formation and properties of gluon-quark plasma in heavy ions collisions.

The unique energy and luminosity reach of the LHC allows a large range of physics opportunities for the general-purpose experiments, such as ATLAS and CMS. Their main original focus was to study the origin of the spontaneous symmetry-breaking mechanism in the electro-weak sector of the SM. "Other important goals are the searches for heavy W- and Z-like objects, for supersymmetric particles, for compositeness of the fundamental fermions, as well as the investigation of CP-violation in B-decays, and detailed studies of the top quark" [13]. The required sensitivities to a wide variety of final states (electrons, photons, muons, tau-leptons, jets, b-jets, etc) drove detector designs.

In the past ten years I have worked on the ATLAS experiment. This manuscript is the summary of this work.

[1] Data-taking with Heavy Ions is also possible, but not discussed in this manuscript.

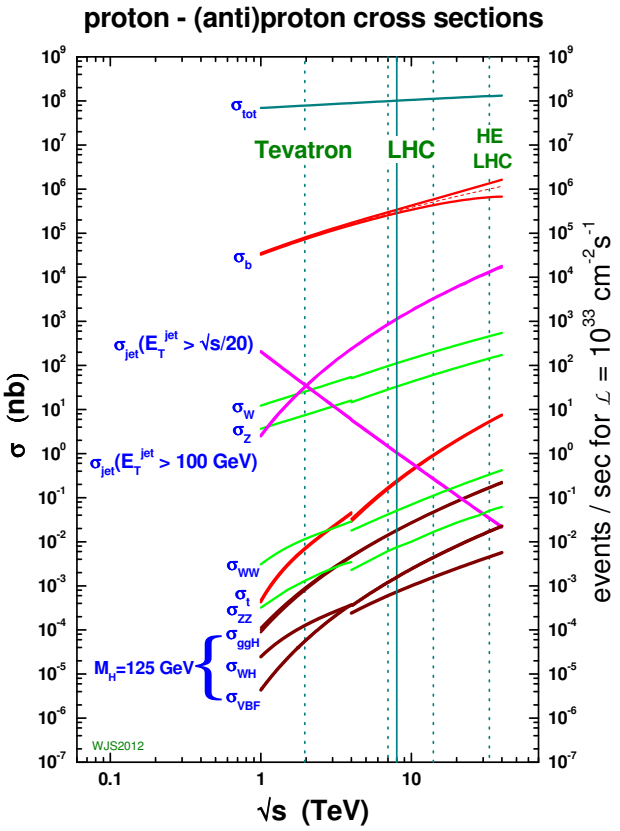

Figure 1.2: Cross sections for various SM processes as a function of the centre-of-mass energy. From [14].

My main interest on joining ATLAS was its potential to discover new physics phenomena. For various reasons outlined later my personal involvement centers on the searches for the resonant structures in the dielectron final state. At the same time I was exposed to the full spectrum of the ATLAS exotics searches through my work on the ATLAS trigger.

The trigger is crucial in the hadronic-collider environment, as the cross-sections for the processes of interest are much lower than the total cross-section, as shown in Figure 1.2. With the design LHC collision rates of the order of few tens of MHz it is not possible to record 100% of the collision events. To efficiently reject the high-rate backgrounds online, while maintaining excellent and unbiased efficiency for even the rare signals poses huge challenges to the trigger. How to decide which events to record and which not, making sure that no interesting signals (potentially from the new physics channels, which we have not thought of yet!) are missing, has been my major preoccupation in the last ten years.

Chapter 2 introduces the experimental apparatus: the LHC, the ATLAS detector and basic object reconstruction. Chapter 3 describes the ATLAS trigger and how we decide which data to collect. Chapter 4 describes my quest in search for the new phenomena in the dilepton final state and Chapter 5 outlines some ideas which I would like to explore in the future.

Chapter 2

Experimental Setup

2.1 The Large Hadron Collider

The Large Hadron Collider (LHC) [15] at the European Organization for Nuclear Research (CERN) is a 27 km circular collider. Its energy reach is limited by its maximum magnetic field (8 T). This magnetic field, used to steer the particles around the ring, is provided by 1232 superconducting NbTi dipole magnets cooled to a temperature of 1.9 K. The LHC is designed to operate at the proton-proton center-of-mass energies of up to 14 TeV and the nominal luminosity of 10^{34} cm^{-2} s^{-1}.

The LHC beam parameters, beam sizes and beam intensities are determined by the performance of its injector complex. First protons are extracted by ionizing hydrogen atoms and fed into a linear accelerator, Linac-2 which accelerates them to 50 MeV. Then the Booster and the proton synchrotron (PS) are used to prepare the proton bunches and to accelerate them to 25 GeV, the injection momentum of the super proton synchrotron (SPS). Finally the beam is injected from the SPS into the LHC ring at 450 GeV.

The LHC can be operated with different filling schemes which have to meet certain requirements. There is always a window of at least 119 empty bunches, called *abort gap* to allow for the beam-dump-kicker rise-time. In total there are 3564 possible bunch positions spaced at 25 ns prepared in the PS. The SPS can provide bunch trains consisting of 72 bunches each and with spacing of 8 bunches corresponding to the SPS-injection-kicker rise-time. Those bunch trains are combined into batches of 3 or 4 with either 38 or 39 bunch spacing to allow for the LHC-

Table 2.1: Evolution of the typical LHC settings at Interaction Points 1 and 5 with time.

Year	Energy [TeV]	Peak Luminosity [10^{33} cm^{-2} s^{-1}]	Integrated Luminosity	Number of average pile-up events	Bunch-spacing [ns]
Design	14	10	-	23	25
2009	0.9/2.36	7×10^{-7}	$\sim 12-20\mu$b^{-1}	-	
2010	7	0.2	48.1 pb^{-1}	2	150
2011	7	3.7	5.46 fb^{-1}	9	50
2012	8	7.7	22.8 fb^{-1}	23	50
2015	13	5.2	4.2 fb^{-1}	14	25

injection-kicker rise-time. Thus the maximal number of bunches which can be put into the LHC is 2808 filled bunches with 25 ns spacing or 1380 with 50 ns spacing.

At the four LHC interaction points the two beams are brought into collision. With more than 10^{11} protons per LHC bunch at the design luminosity and bunch-spacing there should be on average 23 interactions per bunch-crossing (pile-up).

The LHC started single beam operations in 2008 and achieved first collisions in 2009. Typical LHC operating conditions are summarized in Table 2.1. They can be split into a few distinct periods:

- **Run 1** covers lower energy data-taking up to early 2013.
- **Run 2** covers data-taking at energies of 13 TeV and above which started in 2015 and will continue till the end of 2018.
- **Run 3 (Phase 1)** is expected to start in the beginning of 2021. Its main feature should be the LHC luminosity reaching twice its nominal design value (2×10^{34} cm^{-2} s^{-1}) inducing 60 interactions per bunch-crossing on average.
- **High-Luminosity LHC Run (Phase 2)** is expected to start in the end of 2026. Its main feature should be the LHC luminosity increase to 5×10^{34} cm^{-2} s^{-1}and about 140 interactions per bunch-crossing on average.

The data-taking periods are interleaved with the long-shutdown periods (LS):

- **LS1** (2013-2015) was used for the consolidation of the machine elements to achieve design beam energy and luminosity.
- **LS2** (2019-2020) is planned for the upgrade of the injector system.
- During **LS3** (2024-2026) the LHC plans major upgrade to its components (installation of the new focusing quadropoles, crab cavities in the interaction regions etc.).

Each LHC improvement (either luminosity or energy increase) offers a major gain in physics potential through increasing sensitivity to higher-mass or lower-cross-section processes. For the LHC detectors those increases in physics potential come with considerable challenges as the increased luminosity brings much higher levels of pile-up events, radiation etc. To exploit maximally the new physics reach and preserve its physics acceptance the ATLAS detector will undergo a series of upgrades as will be discussed later in this manuscript.

2.2 The ATLAS Detector Overview

The ATLAS [16] experiment at the LHC is a multi-purpose particle detector.

Its broad physics program, ranging from precisions SM measurements to searches for the SM Higgs boson and the new physics phenomena, requires precise identification and measurements of charge and momenta over a wide range for electrons, muons, photons, b-jets, tau-leptons and jets, placing stringent requirements on the detector design. The variety of signatures is important in the high-rate environment of the LHC in order to achieve robust and redundant physics measurements with the posibility of internal cross-check. Large acceptance in pseudorapidity with

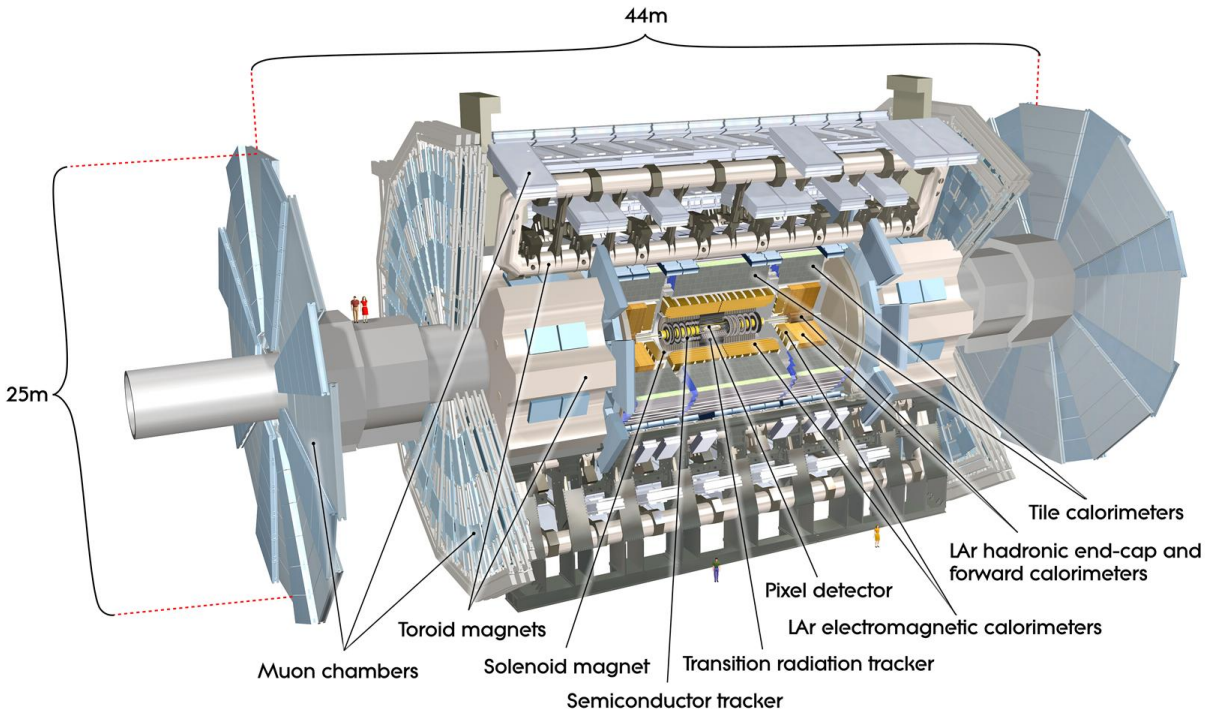

Figure 2.1: The ATLAS detector. [16]

almost full azimuthal-angle coverage is crucial for the missing transverse energy measurements, providing sensitivity to any particles which do not interact in the detector.

Due to the experimental conditions of the LHC, every candidate event is accompanied by other inelastic events in the same bunch crossing, averaging 23 events at the nominal luminosity. This overlap of pile-up events can be reduced by using highly granular detectors with good time resolution, giving low occupancy at the expense of having a large number of detector channels. High particle fluxes emanating from the interaction region lead to high radiation levels, requiring radiation-hard sensors and electronics.

The overall ATLAS detector layout is shown in Figure 2.1. It has a cylindrical geometry[1] covering almost the entire solid angle around the interaction point. The detector components are described as *barrel* if they are in the central region of pseudorapidity or *endcap* if they are in the forward regions.

Starting from the interaction point, the *Inner Tracking Detector* (*ID*) consists of a three layer silicon *pixel* detector in the barrel (three disks in the endcaps), microstrip detector called *SemiConductor Tracker, (SCT)* with the four-layers in the barrel (9 disks in the endcaps) and straw-tube tracking detector with transition radiation capability (*Transition Radiation Tracker, TRT*) surrounding it. For Run 2, a new pixel layer (*Insertable B-layer, IBL*) has been added at

[1] ATLAS uses a right-handed coordinate system with its origin at the nominal interaction point (IP) in the center of the detector and the z-axis along the beam pipe. The x-axis points from the IP to the center of the LHC ring, and the y-axis points upward. Cylindrical coordinates (r, ϕ) are used in the transverse plane, ϕ being the azimuthal angle around the z-axis. The pseudorapidity is defined in terms of the polar angle θ as $\eta = -\ln\tan(\theta/2)$.

a radius of 3.3 cm. Both the Pixel and SCT cover the region $|\eta| < 2.5$, while the TRT covers $|\eta| < 2.0$. The magnetic field for the inner tracking is provided by a thin superconducting solenoid generating field of 2 T.

The electromagnetic (EM) calorimeter is a lead-liquid argon (LAr) sampling calorimeter with an accordion geometry, divided into a barrel section covering the region $|\eta| < 1.45$ and two endcap sections (EMEC) covering the region $1.375 < |\eta| < 3.2$. The EM calorimeter has three longitudinal layers:

- The first layer has a thickness of $3-5$ radiation length and a high granularity in η, providing discrimination between single photons and photon pairs from π^0 decays in jets.
- The second layer collects most of the EM shower energy and has thickness of about 17 radiation length and a granularity 0.025×0.025 in $\eta \times \phi$.
- The third layer collects the tail of the shower and has a coarser segmentation, allowing to discriminate between electrons and hadrons (e.g. $\pi^{\pm}$).

The central EM calorimeter has a thin pre-sampler layer at $|\eta| < 1.8$ to correct for upstream energy losses. In the endcap LAr technology is used for the hadronic calorimeter. The forward regions are instrumented with LAr calorimeters for both EM and hadronic energy measurements up to $|\eta| = 4.9$. Those detectors are housed in one barrel and two endcap cryostats. The barrel of the hadronic calorimetry ($|\eta| < 1.7$) is provided by an iron-scintillator tile sampling calorimeter using wavelength-shifting fibers.

The calorimetry is surrounded by the muon spectrometer (MS) mounted in and around air core toroids that generate an average field of 0.5 T in the barrel and 1 T in the endcap regions. Precision tracking information is provided by three stations of *Monitoring Drift Tubers (MDT)* in the region $|\eta| < 2.7$ (2.0 for the innermost layer) and by *Cathode Strip Chambers (CSC)* in the region $2.0 < |\eta| < 2.7$. First level trigger uses information from the *Resistive Plate Chambers (RPC)* in the barrel ($|\eta| < 1.05$) and the *Thin Gap Chambers (TGC)* in the endcaps ($1.05 < |\eta| < 2.4$).

The *online* event selection must reduce the billion interactions per second to a few hundred events per second for storage, without any loss of interesting physics events. The ATLAS trigger system consists of two main levels: a hardware based Level 1 (L1) and a software-based High-Level-Trigger (HLT). It is described in detail in the next chapter.

The detector has operated with efficiencies exceeding 99.6% per subsystem in the 2012 run (95.5% of events all good for physics) and with performance characteristics very close to its design values.

2.3 Object Reconstruction

This section briefly discusses objects used in dilepton physics analysis: electrons and muons.

2.3.1 Electrons

Only electrons within the inner-detector acceptance (e.g. $|\eta| < 2.47$) are considered in this manuscript. More detailed overview of electron reconstruction, identification and calibration can be found in Refs. [17, 18, 19].

Energy reconstruction in the LAr calorimeter

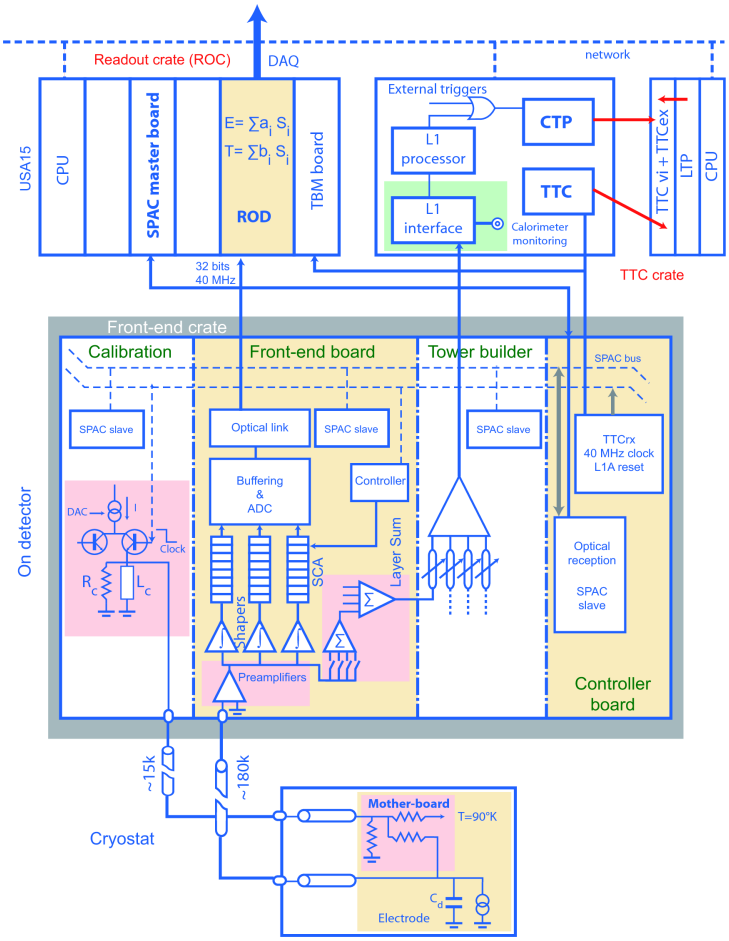

Figure 2.2: The current LAr readout electronics architecture from Ref. [20].

Charged particles from EM shower ionize the liquid argon in the calorimeter. Under the influence of the electric field, the ionization electrons drift towards the electrode inducing a current, which is proportional to the energy deposited in the liquid argon.

The current LAr readout electronics architecture is shown in Figure 2.2. As one can see there are two separate read-out paths: one with coarse granularity (*Trigger Towers*) used for the first-level of the trigger and one with fine granularity used by the high-level-trigger and offline reconstruction. The description below concentrates on the latter.

Inside a front-end-board (FEB), the signal is first pre-amplified. Then shaper splits output signal into three overlapping linear gains: high (gain ratio=82), medium (gain ratio=8.4), and low (gain ratio=0.8) to cover energies ranging from a few TeV down to the noise level. Figure 2.3 shows a typical triangular pulse shape of the ionization signal along with the shaped and sampled signal shape. The output shaped signal is sampled at 40 MHz and, for events selected by the L1 trigger, five[2] samples around the peak spaced by 25 ns are extracted and sent to a 12-bit

[2]In Run 2 only four samples are used to allow higher L1 trigger rate.

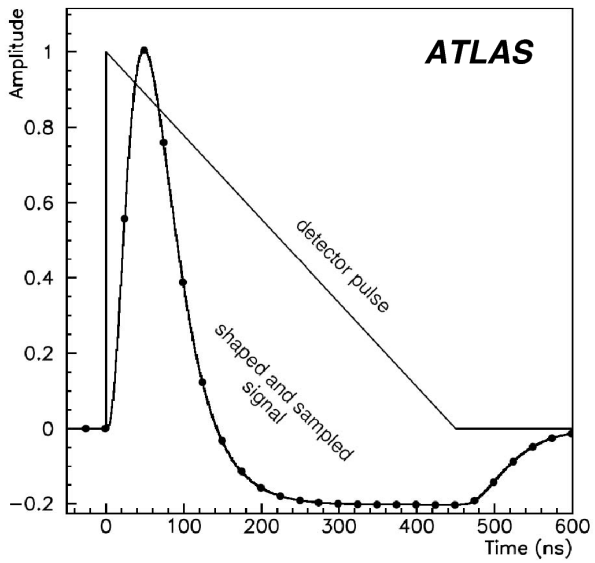

Figure 2.3: The amplitude vs. time for the triangular pulse shape from the LAr calorimeter, overlaid with the bipolar-shaped and sampled pulse shape (from Ref. [20]).

analog-to-digital converter (ADC).

The Readout Driver (ROD) modules receive raw data from the FEBs and use the Optimal Filtering method to calculate the amplitude of the pulse (A, ADC counts) and the difference between digitization time and the chosen phase (Δt, ns):

$$A = \sum_{i=0}^{n} a_i(s_i - p), \tag{2.1}$$

$$\Delta t = \frac{1}{A}\sum_{i=0}^{n} b_i(s_i - p), \tag{2.2}$$

where a_i and b_i are the Optimal Filtering Coefficients (OFCs) computed per cell from the predicted ionization pulse shape and the measured noise autocorrelation to minimize the noise and pile-up contributions, s_i are the samples, p is the electronic pedestal and n represents the number of samples used.

Note that if the samples are shifted in time, this leads to wrong computation of OFCs. For example, a time shift corresponding to ~ 5 ns leads a 0.5% bias on the energy reconstruction. Precise measurement of the time of the signal peak is also a valuable input for exotic particle searches with a long lifetime or for very massive stable particles. The timing can be influenced by various factors (the length variation of the optical fibers delivering the LHC clock to the ATLAS experiment due to temperature change, wrong calorimeter high-voltage module settings, FEB internal delays, different cable length for each FEB etc.). Some of those factors are constant and were corrected for in the beginning of data-taking, but others could change with time and thus have to be monitored constantly. The timing alignment of the LAr calorimeter cells was better than 1 ns in 2011 [21] and better than 500 ps [22] in 2012.

The stability of the electronic response of the readout cells (i.e. pedestal, noise and gain) is regularly monitored using dedicated calibration runs. The pedestal and noise for each cell are

computed in the dedicated daily Pedestal calibration runs as the mean of the signal samples s_i in ADC counts and the width of the energy distribution, respectively. The same runs also provides information on the noise auto-correlation needed for the OFC coefficient calculation. In so-called Ramp and Delay calibration runs, calibrated current pulses are injected through high-precision resistors to simulate energy deposits in the calorimeters and the corresponding cell responses are reconstructed. Ramp runs are used to measure the gain (G) as well as the factor $F_{DAC\to\mu A}$ which converts digital-to-analog converter (DAC) counts set on the calibration board to μA. The weekly Delay runs measure the full calibration pulse shapes. The results of those calibration runs are analyzed and if any differences with respect to reference values are observed the online database is updated so that correct values can be used for the energy calculation.

Including the relevant electronic calibration constants, the deposited energy (in MeV) is determined as:

$$E_{cell} = F_{\mu A\to \text{ MeV}} \times F_{DAC\to\mu A} \times \frac{1}{\frac{M_{phys}}{M_{cali}}} \times G \times A, \tag{2.3}$$

where the factor $\frac{1}{\frac{M_{phys}}{M_{cali}}}$ quantifies the ratio of response to a calibration pulse and an ionization pulse corresponding to the same input current and the factor $F_{\mu A\to \text{ MeV}}$ is estimated from simulations and beam test results.

Offline Electron Reconstruction and identification

Electron reconstruction starts with a creation of an EM cluster using a sliding-window algorithm with size of 3×5 cells in (η, ϕ) space in the middle calorimeter layer from energy deposits with total $E_{\text{T}} > 2.5$ GeV. Tracks reconstructed in the inner detector with $p_{\text{T}} > 0.5$ GeV are extrapolated to the calorimeter and matched to the EM cluster. An electron is considered to be reconstructed if at least one track is matched to the cluster. Matched clusters are then rebuilt with a slightly larger window, 3×7 in the barrel or 5×5 in the endcap.

In Run 1 a cut-based selection was used for the electron identification. It has sequential cuts optimized in cluster-$\eta \times E_{\text{T}}$ bins on calorimeter shower-shapes, tracking, track-cluster matching and TRT-identification variables. For the list of the selection variables please see Ref. [17]. The selection exploits the fact that the shower development is narrower and shorter for electrons than for hadrons. There are at least three nested sets of selection criteria, labeled *loose, medium and tight* with increasing background-rejection power obtained by adding discriminating variables at each step and by tightening the selection on the initial variables.

The electron selection evolved with time. For example in 2009-2010 electron selection at all levels tended to be rather loose focusing on robustness as the detector was still undergoing commissioning with the first LHC data. For 2011, electron selection needed to be tightened considerably to increase background rejection power in the much higher pile-up conditions and minimize its pile-up dependence. For more details on the 2011 configuration see Ref. [19]. In 2012, electron tracking was improved offline [23] with the introduction of the Gaussian Sum Filter algorithm which accounts for the non-linear bremsstrahlung effects. Electron selection had to be re-tuned again to remove the residual pile-up dependences.

For Run 2 electron identification moved from the more robust cut-based to more performant likelihood-based identification criteria maintaining the same selection variables. Generally the likelihood-based selection provides about a factor two improvement in background rejection for the same signal efficiency with respect to the optimized cut-based electron selection.

The electron four-momentum is built from the cluster energy and the direction of the associated track from the ID. The final cluster energy is obtained by correcting for the energy losses in the material in front of the calorimeter, the lateral leakage due to the fixed cluster size and the longitudinal leakage to the hadronic calorimeter.

2.3.2 Muons

This information is provided for completeness. I have not performed any work on the muon reconstruction, but muons were used in the analysis presented later. More detailed overview of muon reconstruction and identification can be found in Ref. [24].

In Run 1 several types of algorithms for reconstructing muons were available in ATLAS. Most analysis use so-called combined muons: track reconstruction is performed independently in the ID and MS, and a combined track is formed from the successful combination.

There are various ways to do this combination, for example one can perform a statistical combination of the track parameters of the stand-alone and the ID muon tracks using corresponding covariance matrices (Chain 1). One can also perform a global refit of the muon track using hits from both the ID and MS sub-detectors (Chain 2). The use of two independent codes provided redundancy during commissioning phase, but caused problems as there there was non-negligible non-overlap between the reconstructed muon candidates as discussed in Section 4.3. A unified reconstruction program has been developed in 2012 to be used for the future data-taking.

In addition to the standard muon selection, requiring a minimum number of hits in each of the ID components etc. exotics searches with high-p_{T} muons applied a special high-p_{T} muon selection detailed in Ref. [25]. Muon momentum is taken from combined fit.

2.4 My contributions

- In 2008-2010 I was responsible for the documentation of the ATLAS electron and photon performance group summarizing object reconstruction, selection variables, calibration procedures, etc. on the web and in the code (doxygen).
- In 2011 I was a member of the LAr electronics calibration team responsible for the validation of the calibration runs.
- In 2009-2011 I supervised Ludovica Aperio-Bella's work on the LAr timing alignment [21]. She developed the LAr cells timing methodology and achieved the global LAr timing alignment below the one ns for all the LAr partitions, and the EM barrel time resolution below the 1 ns level.

Chapter 3

ATLAS Trigger and Trigger Menu

This chapter discusses ATLAS trigger developments over the past ten years. This overview concentrates on the aspects I worked on. Its focus varies with the evolution of my responsibilities within the trigger group.

3.1 Introduction

Nominal LHC bunch-spacing is 25 ns. This means that every 25 ns there could be a potentially interesting event which needs to be recorded. Each event has a size of ∼1 Mb - thus it is not possible to store 100% of the events. The multi-level trigger system reduces the 40 MHz sampling rate to a few hundred Hz of events for offline reconstruction and physics analysis. Each trigger level refines the decisions made at the previous level and, where necessary, applies additional selection criteria. Each trigger level has its own constraints (timing, output rate[1], etc.) which change during the lifetime of the experiment, as summarized in Table 3.1, to preserve the physics acceptance despite the LHC luminosity increases.

Stable operation of the trigger is crucial as many parts of the system constitute a single point of failure, with problems potentially leading to loss of physics data. Detailed monitoring and thorough testing of any modifications are essential to ensure the smooth data-taking.

[1]Note that while usually the peak rate provides main constraint for the trigger, for the last level of the trigger the main constraint comes from the average output rate. In a fill with a certain peak luminosity, trigger rates follow the luminosity decrease with time. In general it was noted that the average luminosity in a typical run is about 2/3 of the peak luminosity. Thus peak rate = 1.5× average rate.

Table 3.1: Trigger Rate Evolution. Maximum L1 accept rate which the detector readout systems can handle in Run 1 was 75 kHz, upgradable to 100 kHz. High Level Trigger (HLT) in Run 1 consisted of two separate levels: Level 2 (L2) and Event Filter (EF).

	Design	Run 1	Run 2
peak L1 Rate (kHz)	75(100)	65	90
peak L2 Rate (kHz)	3.0	5.5	-
average HLT (EF) Rate (Hz)	200	400	1000

The trigger system is configured via the *trigger menu*. The trigger menu specifies which event selection algorithms are enabled and thus it is of critical importance for the physics program of ATLAS. The menu should provide efficient coverage to all physics processes of interest from the SM measurements to the searches for physics beyond the SM, including everything we have not yet thought of. If a physics signal does not have a trigger matched to its signature, it would not be possible to do the corresponding analysis or the analysis would have suboptimal sensitivity.

The trigger menu is designed to have the best possible physics sensitivity at a given luminosity while keeping trigger rates, CPU consumption etc. within the resource limitations of the trigger and data acquisition system (DAQ). In order to provide a coherent dataset for physics analyses, the trigger menu has to be as stable as possible.

To address those somewhat conflicting requirements and decide on the final configuration of the trigger menu, the ATLAS Collaboration has a dedicated Menu Coordination Group (MCG). It is led by Trigger Menu Coordinators and consists of ATLAS management, physics, data-preparation and run coordinators, trigger management as well as representatives from all the combined performance and physics analysis groups (about 20-30 people in total). Most of my trigger activities described in this manuscript have been performed as a member of this group.

The rest of this chapter is constructed as follows: a general overview of the ATLAS trigger (Section 3.2) is followed by the description of the trigger system in Run 1 (Section 3.3) and the Run-1 menu development time-line (Sections 3.4-3.5). Section 3.6 describes updates of the trigger system for the Run 2. Section 3.7 reviews the Run 2 trigger menu and the last two sections provide conclusions and summarize my contributions in the domain of the trigger.

3.2 ATLAS Trigger Overview

3.2.1 First Level Trigger

The first level trigger (L1) is based on fast, custom electronics using low-granularity signals from the calorimeters (L1Calo) and fast signals from dedicated muon trigger chambers (L1Muon). The main available L1 trigger signatures and their maximum number of the L1 thresholds are shown in Table 3.2.

L1 Calorimeter Trigger

The L1Calo trigger is based on inputs from the electromagnetic and hadronic calorimeters covering region $|\eta| < 4.9$. It provides triggers for signals consistent with a high transverse momentum electron/photon, tau and jet or large missing transverse energy ($E_{\mathrm{T}}^{\mathrm{miss}}$). The L1Calo trigger threshold[2] is applied to a transverse energy (E_{T}).

L1 Muon Trigger

The L1 muon trigger system identifies muons by the spatial and temporal coincidence of RPC and TGC hits. The degree of deviation from the hit pattern expected for a muon with infinite momentum is used to estimate the p_{T} of the muon at six possible thresholds. The L1 triggers generated by hits in the RPC require a coincidence of hits in the three layers for the highest three

[2] It is possible for the calorimeter threshold to be pseudorapidity dependent to take into account the energy loss in the detector material before the calorimeter (denoted by "V"in the trigger names).

Table 3.2: The key trigger objects identified by the trigger system, their shortened representation used in the trigger menus and the number of the L1 thresholds available for each of the object types.

	Representation		Number of L1 Thresholds		
Trigger signature	L1	HLT	Design	Run 1	Run 2
electron	EM	e	8	9	16
photon	EM	g	as above	as above	as above
muon	MU	mu	6	6	6
jet	J	j	12	12	25
tau	TAU	tau	8	7	16
$E_{\mathrm{T}}^{\mathrm{miss}}$	XE	xe	8	8	8
$E_{\mathrm{T}}^{\mathrm{miss}}(\lvert\eta\rvert < XX)$	XE.0ETAXX	xe.0etaXX	-	-	8
$\sum E_{\mathrm{T}}$	TE	te	4	4	8
$\sum E_{\mathrm{T}}(\lvert\eta\rvert < XX)$	TE.0ETAXX	te.0etaXX	-	-	8
total jet energy	JE	je	4	4	-
$E_{\mathrm{T}}^{\mathrm{miss}}$significance	XS	xs	-	8	8
b-jet	-	b	-	-	-

p_{T} thresholds, and a coincidence of hits in two of the three layers for the other three thresholds. The L1 triggers generated by hits in the TGC require a coincidence of hits in the three layers, except for limited areas in the lowest threshold.

Central Trigger Processor

The information from L1Calo and L1Muon systems is sent to the Central Trigger Processor (CTP), where it is combined and the result is compared to the pre-programmed L1 trigger items. The maximum allowed number of the L1 trigger items (256 in Run 1 and 512 in Run 2) as well as their possible AND/OR combinations are fixed by the CTP hardware. If the trigger conditions are met, a L1 Accept is issued initiating the detector readout. The maximum L1 accept rate is limited by the detector readout system to be about 75 kHz in Run 1, upgradable to 100 kHz. The L1 trigger decision must reach the front-end electronics within 2.5 μs after the bunch crossing it is associated with.

3.2.2 High Level Trigger and Trigger Menu Overview

The High Level Trigger (HLT) is software-based and runs on large PC-farms. The HLT receives the L1 trigger decision together with information on so-called Regions-of-Interest (RoIs) around the L1 objects. The RoI information is used to perform regional event reconstruction. In addition, the full detector event data is available to the HLT as needed. HLT has a few seconds to decide if an event should be kept or not and its *average* output rate is limited by the offline computing resources available for the data storage and processing.

A trigger selection is organized into so-called *trigger chains*, each consisting of one specific L1 selection seeding a sequence of selection algorithms in the HLT. Each chain is responsible for selecting a specific physics signature. An example of a single electron trigger chain is discussed

in Section 3.4.1.

Further flexibility is provided by defining bunch groups, which allow trigger chains to include specific requirements on the LHC bunches colliding in ATLAS. These requirements include paired (colliding) bunch-crossings for physics triggers, empty or unpaired crossings for background studies and dedicated bunch groups for detector calibration.

A full selection of the trigger chain is encoded in its trigger name which consists of the trigger level, multiplicity, particle type (specified in Table 3.2) and p_{T}-threshold value in GeV (e.g. L1_2MU4, HLT_mu40). The L1 objects are written in capital letters and a trigger name without level prefix refers to the entire trigger chain. Further selection criteria (tightness or type of identification, isolation, reconstruction algorithms, etc.) applied to a given trigger object at the HLT are appended to the trigger name (e.g. g120_loose is a 120 GeV photon trigger with a loose selection applied to photon objects). In case of ambiguity, the L1 seed is also suffixed to the trigger name (e.g. e24_lhmedium_L1EM20VH). Triggers executed without a requirement on the L1 seed have "noL1" attached to their p_{T}-threshold value.

There are four different classes of trigger chains:

- Single-object triggers: used for final states with at least one characteristic object.
- Multi-object triggers: used for final states with two or more characteristic objects of the same type.
- Combined triggers: used for final states with two or more characteristic objects of different types. For example, a 60 GeV photon plus 60 GeV $E_{\mathrm{T}}^{\mathrm{miss}}$ trigger with no L1 $E_{\mathrm{T}}^{\mathrm{miss}}$ requirement would be denoted g60_loose_xe60noL1.
- Topological triggers: used for final states that require selections based on information from two or more RoIs. For example the mu6_j150_dr05 trigger for b-jet calibration studies requires a 150 GeV jet and a 6 GeV muon to be within $|\Delta R| < 0.5$ of each other.

The full set of trigger chains is called the trigger menu. A typical menu contains around one thousand chains. It includes not only a few hundred primary physics chains, but also a large set of *support* triggers to allow background and efficiency measurements as well as monitoring and calibration triggers which collect data to ensure the correct operation of the trigger and detector.

Prescale factors can be applied to each L1 and HLT trigger, such that on average only 1 in N events passing the trigger causes an event to be accepted at that trigger level. Prescales can also be set so as to disable specific chains. Prescale values can be changed during data-taking to ensure the optimal trigger menu for a given LHC luminosity. Trigger menu *prescale sets* determine the exact menu configuration which is run online.

Data for events selected by the trigger system are written to *inclusive data streams*[3]. Table 3.3 provides a list of main streams and their typical event size. *Physics* streams contain information from the whole detector. About 10-20 Hz of those physics events are also written to an *express* stream where prompt offline reconstruction provides calibration and Data Quality information prior to the reconstruction of the other physics streams. There are about a dozen additional streams for calibration, monitoring and detector performance purposes. Some of these streams use partial event building to record only the relevant sub-detector data, thus decreasing the event size significantly. Any events for which the trigger is unable to make a decision because of the

[3] *Inclusive* means that an event which passes requirements for multiple data streams is recorded in all of them.

Table 3.3: Trigger streams and their average (compressed) event size per event in 2015.

Stream	Purpose	Event size [kB]
Main	Physics analyses	805
Express	Prompt calibration and DQ	810
Jet TLA	Trigger-level dijet search	3
L1Calo, CosmicCalo	Calorimeter studies	814, 904
TauOverlay, ZeroBias	MC simulation	1700
LArCellsEmpty, LArCells	LAr detector calibration	35, 73
LArNoiseBurst, TGCNoiseBurst	Identify noise bursts in various detectors	880, 760
PixelNoise, SCTNoise	Noise of the silicon detectors	29
IdTracks	ID alignment	16
Muon	Muon alignment	1
Tile	Tile calorimeter calibration	181
Beamspot	Online beamspot determination	325
CostMonitoring	HLT system performance information	114
PixelBeam	ID data for luminosity measurement	96

trigger time-out or any other failure in the online software, are recorded to a special stream called *debug stream*. Those events can be later re-analyzed offline.

3.3 Prehistory: ATLAS Trigger System in Run 1 and "Design" Trigger Menu

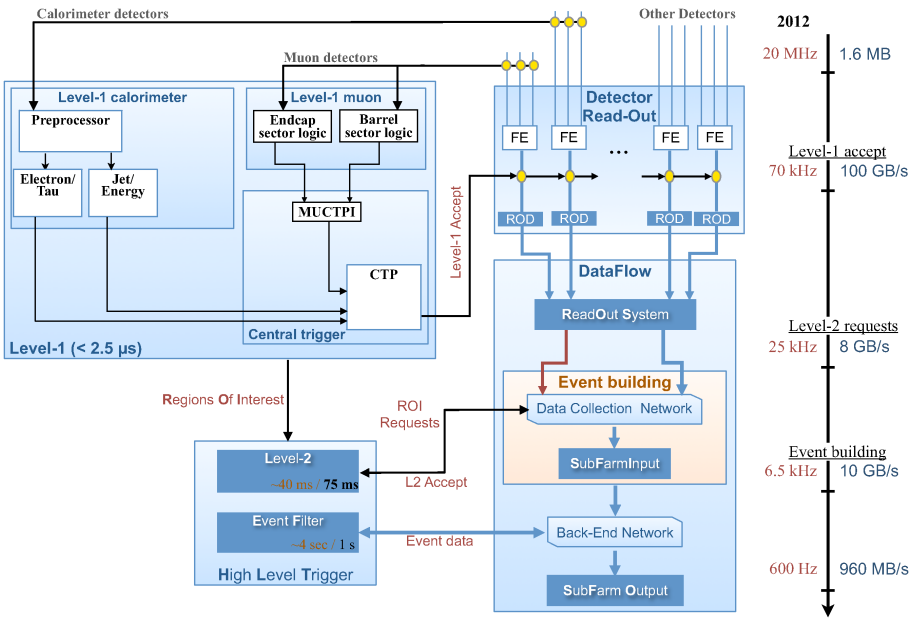

Figure 3.1: Overview of the ATLAS trigger and DAQ system in 2012 [26].

The ATLAS trigger system design layout is shown in Figure 3.1. This architecture was

unchanged for the whole Run 1. As shown in the figure, the original design assumed a three-level system with a hardware-based L1 followed by an HLT consisting of two software-based levels: Level-2 (L2) and Event Filter (EF). L1 reduced the 40 MHz sampling rate to 75 kHz in 2 μs. In Run 1 L2 was running customized fast algorithms and requesting the data for the relevant detectors based on the RoIs defined by the L1. It had to make a decision in about 40 ms and reduced rate to about 2-5 kHz. The EF reduced rate to 200 Hz in about 4 seconds and used offline reconstruction algorithms adapted for the trigger in order to achieve the best performance on the full event data.

Table 3.4: Original L1 and L2 low and high luminosity menu for center-of-mass energy of 14 TeV. Note that this menu uses special naming convention. The calorimeter threshold values correspond to the point where L1 (L2) algorithms are 95%(90%) efficient. For the $E_{\mathrm{T}}^{\mathrm{miss}}$ trigger the threshold value corresponds to the cut. The muon thresholds correspond to a point of 90% efficiency at L1, not accounting for inefficiency due to the limited detector coverage.

L1 Trigger	L1 Rate (kHz)	L2 Trigger	L1 Trigger	L1 Rate (kHz)	L2 Trigger
Low Luminosity			High Luminosity		
MU6	23	mu20	MU20	3.9	mu20i
		mu6_Bphys	2MU6	1	2mu6_Bmumu
					2mu10
		mu6i_e15i	EM15I_MU10	0.4	e15i_mu10i
EM20I	11	e20i	EM30I	22	e30i
		g40i			g60i
2EM15I	2	2e15i	2EM20I	5	2e20i
		2g20i			2g20i
J180	0.2	j180	J290	0.2	j290
3J75	0.2	3j75	3J130	0.2	3j130
4J55	0.2	4j40	4J90	0.2	4j90
J50_XE50	0.4	j50_xe50	J100_XE100	0.5	j100_xe100
TAU20_XE30	2	tau20_xe30	TAU60_XE60	1	tau60_xe60

The first set of ATLAS trigger menus appeared in 1998 [27] and was refined in 1999 [28]. These menus shown in Table 3.4 addressed two scenarios: low luminosity (10^{33} cm^{-2} s^{-1}) and high luminosity (10^{34} cm^{-2} s^{-1}) at $\sqrt{s} = 14$ TeV aiming at about 40 kHz at L1 and about 2000 Hz at L2.

It can be noted that even this rather limited set of triggers covers a significant portion of the physics goals of the ATLAS experiment. In particular the inclusive lepton and dilepton triggers provide $W \to l\nu$ and $Z \to ll$ selections, where l designates electron or muon, giving unbiased triggers for many SM and BSM searches which have those gauge bosons in their final state as well as covering other multi-lepton final states.

The diphoton trigger (2g20i) is targeting the very important $H \to \gamma\gamma$ channel and would be useful for searches for $HH \to bb\gamma\gamma$ or other Higgs-boson-like final states as well as the BSM searches with two or more photons. The inclusive photon trigger proposals are mostly targeting BSM physics with photon thresholds being quite high.

Searches without leptons in the final state (including supersymmetry searches with or without $E_{\mathrm{T}}^{\mathrm{miss}}$) were supposed to be covered by the jet triggers, which had very optimistically low thresholds.

There are only two more special-purpose trigger "lines" in this menu: τ+$E_{\mathrm{T}}^{\mathrm{miss}}$ triggers for the $W \to \tau\nu$ final state (although this would also serve for some supersymmetry searches) and B-physics triggers, which are low p_{T} dimuon triggers with invariant mass or common vertex cuts.

This menu follows the main principle behind the ATLAS trigger menu strategy in the years to come: to keep triggers as general as possible to cover the widest possible range of physics signatures. It is the most long-living ATLAS trigger menu proposal which had survived in its original form for 10 years unchallenged.

3.4 Antiquity: Pre-data-taking ATLAS Trigger Menu

3.4.1 Online electron reconstruction

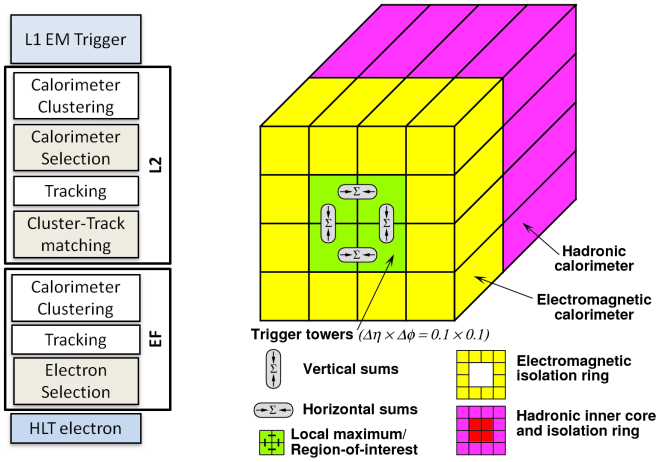

Figure 3.2: (right)Typical Run 1 electron trigger chain. (left) Building blocks of the electron/photon and tau algorithms with the sums to be compared to programmable thresholds. From [29].

One of my first tasks in 2006 when I joined the ATLAS experiment was to optimize the electron trigger selection to minimize an efficiency loss with respect to the offline selection. A typical Run 1 electron trigger chain is shown in Figure 3.2 (left).

First the electromagnetic cluster reconstruction at L1 identifies a Region of Interest as a 2×2 *trigger tower* cluster in the EM calorimeter for which the E_{T}-sum from at least one of the four possible pairs of nearest neighbor towers exceeds a pre-defined threshold as shown in Figure 3.2 (right). Isolation-veto thresholds can be set for the 12-tower surrounding ring in the EM calorimeter (denoted by "I"), as well as hadronic tower sums in a central 2×2 core behind the cluster (hadronic veto, denoted by "H"). The threshold could be set with 1 GeV precision and with $\Delta\eta$ =0.4 granularity.

Seeded by the position of the L1 cluster, the L2 electron selection employs fast calorimeter reconstruction algorithm followed by fast tracking reconstruction. Then, at the EF, further

calorimeter cluster and track reconstruction is performed but using the offline precision reconstruction algorithms. Due to timing constraints the HLT reconstruction algorithms (especially the fast tracking) are less refined than the corresponding offline algorithms leading to potential inefficiencies.

After investigating the sources of efficiency loss it became clear that the leading one was due to differences in variables or cuts between the online and offline selections. Ensuring that the selection at EF was the same or looser than the offline one allowed to increase electron trigger efficiency by approximately 3%.

3.4.2 Development of electron triggers for the low-p_{T} region

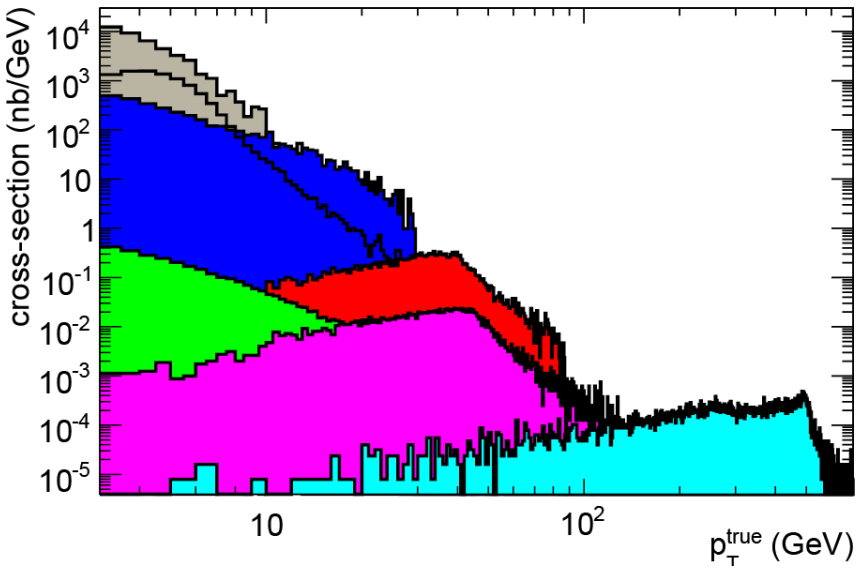

Figure 3.3: A sketch of known and hypothetical potential sources of electrons (e) at the LHC experiments: grey corresponds to $J/\psi \to ee$ decays, open histogram to Υ, blue to $b, c \to e$, red to W, magenta to Z, green to Drell-Yan ($m_{ee} < 60\,\mathrm{GeV}$), cyan (enhansed by a factor of 1000) to 1 TeV Z'.

In early 2007, as data-taking approached a concern was raised about the absence of a trigger menu strategy for the LHC luminosities lower than 10^{33} cm^{-2} s^{-1}. With the unknown LHC start-up schedule, it was not clear how fast we would accumulate sufficient statistics of $Z \to ee$ events for electromagnetic calorimeter commissioning, electron performance studies, etc.

By studying potential sources of electrons, shown of Figure 3.3, it became clear that there should be significant statistics of electrons coming from $J/\psi \to ee$ and $\Upsilon \to ee$ decays. Assuming dielectrons with p_{T}>3 GeV, cross-sections of $pp \to Z : J/\psi : \Upsilon \to ee$ are expected to scale as 2:120:50. Unfortunately as shown in Figure 3.4, most of the signal events are centered at very low electron p_{T}. It is very challenging to trigger on these events at L1, as the L1 calorimeter trigger performance at low-energies is limited by the noise of about 0.5 GeV per RoI. A 3 GeV threshold (EM3) was assumed to be the lowest limit of what is feasible for the L1Calo. The L1 rate studies showed that typical rate of 2EM3 trigger is expected to be 650 kHz at 10^{33} cm^{-2} s^{-1} ($\sqrt{s}$ = 14 TeV) which is much higher than maximal L1 bandwidth. But for lower luminosity points,

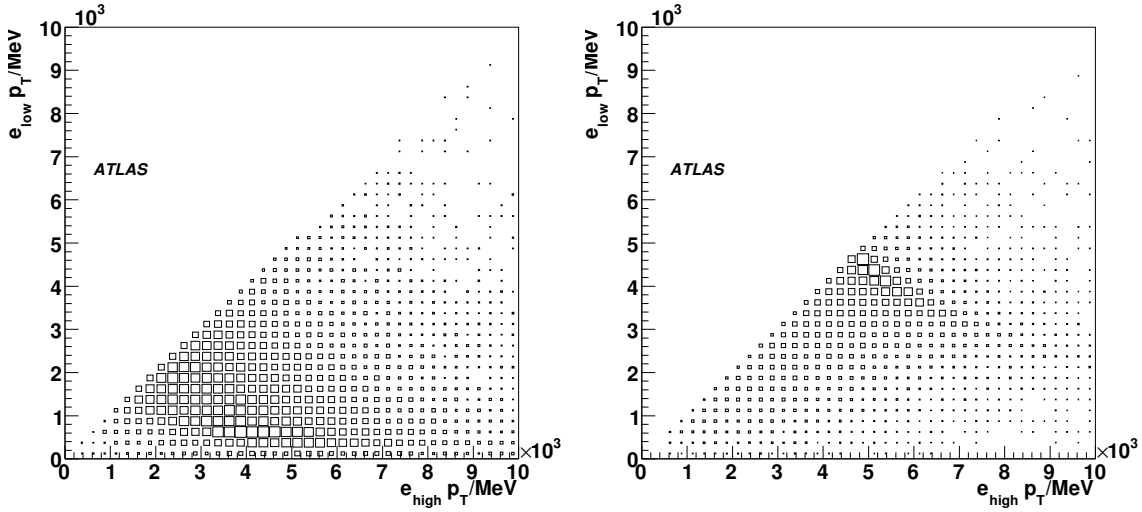

Figure 3.4: Distribution of the generator-level transverse momentum of the less energetic electron versus the transverse momentum of the most energetic electron in the direct J/ψ (left) and Υ (right) decays.

such as 10^{31} cm^{-2} s^{-1}, L1 output rate becomes only 6.5 kHz, which although taking a significant fraction of the total L1 bandwidth, is potentially feasible.

The proposed strategy to trigger on J/ψ and $\Upsilon \to ee$ events was based on two low-E_{T} L1 electromagnetic RoIs and further electron identification using calorimeter and inner-detector information at the HLT. At a luminosity of 10^{31} cm^{-2} s^{-1} this trigger can run unprescaled, which would allow ATLAS to collect about 100k events with J/ψ and 30k with Υ decays in 100 pb^{-1} of data respectively. In the same sample one would expect to collect about 30k of $Z \to ee$ events.

Currently the J/ψ triggers are an essential part of the ATLAS trigger menu even though they are usually prescaled for luminosities above 10^{31} cm^{-2} s^{-1}. One of the electron candidate selections is loosened with respect to the original proposal to enable tag-and-probe studies. It is also not a single trigger but a set of triggers with p_{T}-requirements and tightness of identification criteria varying between the two electrons. The combination of triggers was introduced to allow more uniform event collection as a function of p_{T} as well as enabling tag-and-probe studies. These triggers provide a unique event sample for electron performance studies in the range $7 - 20$ GeV [17], complementing electrons from Z decays which cover the range above 15 GeV. This region of the electron p_{T} is crucial for analyses with multi-lepton final states in general and, in particular, for the observation of the Higgs boson in the $H \to ZZ \to 4l$ channel [10].

3.4.3 2008 trigger menu proposal

In 2008 I was nominated as trigger menu liaison for the electron and photon performance group. My role was to ensure that all the relevant electron and photon triggers needed for performance studies (as well as physics analysis upstream) were present in the ATLAS trigger menu. The J/ψ triggers were one of the main motivations for the creation in 2008 of the 10^{31} cm^{-2} s^{-1} menu shown in Table 3.5. This menu aimed at luminosities a few orders of magnitude below the

Table 3.5: Draft of Trigger menu for center-of-mass energy of 14 TeV and 10^{31} cm^{-2} s^{-1} from Ref. [16]

Signature	L1 Rate (Hz)	HLT Rate (Hz)	Comments
Minimum bias	Up to 10000	10	Pre-scaled trigger item
e10	5000	21	$b, c \to e$, W, Z, Drell-Yan, $t\bar{t}$
2e5	6500	6	Drell-Yan, J/ϕ, Υ, Z
g20	370	6	Direct photons, γ-jet balance
2g15	100	<1	photon pairs
mu10	360	19	W, Z, $t\bar{t}$
2mu4	70	3	B-physics, Drell-Yan, J/ϕ, Υ, Z
mu4+J/$\psi(\mu\mu)$	1800	<1	B-physics
j120	9	9	QCD and other high-p_{T} jet final states
4j23	8	5	Multi-jet final states
tau20i_xe30	5000	10	W, $t\bar{t}$
tau20i_e10	130	1	$Z \to \tau\tau$
tau20i_μ6	20	3	$Z \to \tau\tau$

nominal one and thus allowed for very low-threshold single and di-object unprescaled electron, muon and photon triggers compared to the menu proposal in Table 3.4. This menu introduced hadronic single and ditau triggers to target events from Higgs, W and Z bosons important for SM precision measurements as well as beyond SM processes. Although not mentioned explicitly this menu also included b-jet and missing transverse energy triggers for $t\bar{t}$ measurements and searches of supersymmetry or other exotics particles.

3.5 Middle Ages: ATLAS Trigger Menu 2009 - 2012

3.5.1 Dark Ages: ATLAS Trigger Menu 2009-2010

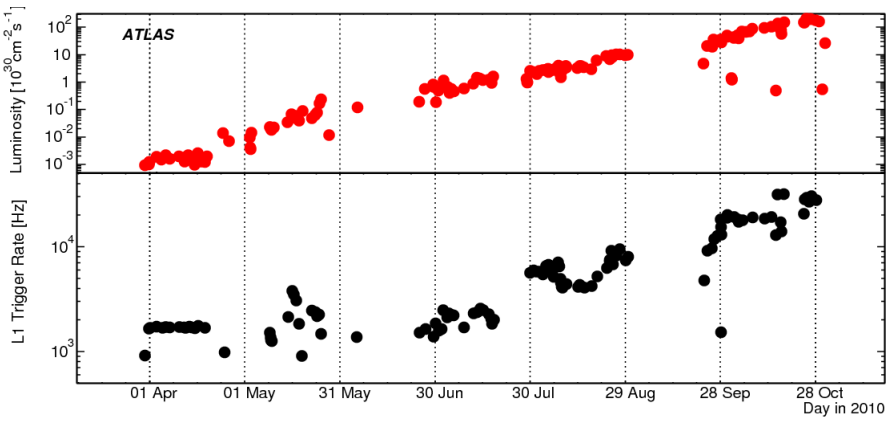

Figure 3.5: Evolution of the L1 trigger rate throughout 2010 (lower panel), compared to the instantaneous luminosity evolution (upper panel) from Ref. [29].

Table 3.6: Examples of p_{T} thresholds and selections for the lowest unprescaled triggers in the 2010 physics menu at center-of-mass energy of 7 TeV from Ref. [29]

Luminosity [$\mathrm{cm^{-2}s^{-1}}$]	3×10^{30}	2×10^{31}	2×10^{32}
Signature	p_{T} threshold [GeV], selection		
Single muon	4	10	13,tight
Dimuon	4	6	6,loose
Single electron	10, medium	15, medium	15, medium
Dielectron	3, loose	5, medium	10, loose
Single photon	15, loose	30, loose	40, loose
Diphoton	5, loose	15, loose	15, loose
Single tau	20, loose	50, loose	84, loose
Single jet	30	75, loose	95, loose
$E_{\mathrm{T}}^{\mathrm{miss}}$	25, tight	30, loose	40, loose
B-physics	mu4_DiMu	mu4_DiMu	2mu4_DiMu

The LHC circulated first beams in 2008 and achieved first collisions in the end of 2009. In 2009 the peak luminosities did not exceed $7\times10^{26}\mathrm{cm^{-2}s^{-1}}$ and center-of-mass energies were 0.9 TeV and 2.36 TeV which corresponds to a few tens of Hz of the trigger rate. The ATLAS trigger could record the full proton-proton collision event rate without any rejection required. The LHC increased its center-of mass energy to 7 TeV in 2010. The luminosity ramp-up was very slow up to the end of that year: increasing from $10^{27}\,\mathrm{cm^{-2}s^{-1}}$ in April 2010, to $10^{30}\,\mathrm{cm^{-2}s^{-1}}$ in June 2010, $10^{31}\,\mathrm{cm^{-2}s^{-1}}$ in August 2010 and finally reaching $2\times10^{32}\,\mathrm{cm^{-2}s^{-1}}$ in October 2010 as shown in Figure 3.5.

This slow luminosity increase allowed time for thorough trigger commissioning as summarized in Ref. [29]. Only when the peak luminosity delivered by the LHC reached $1.2\times10^{29}\,\mathrm{cm^{-2}s^{-1}}$, it was necessary to start enabling HLT rejection for the highest rate L1 triggers.

2010 physics trigger menu designed for $10^{30} - 10^{32}\,\mathrm{cm^{-2}s^{-1}}$ is shown in Table 3.6. The bandwidth allocation between different trigger signatures was driven by their importance for the ATLAS physics program. For example electron/photon and muon triggers were assigned 25% of the bandwidth each while b-jet, B-physics, jets, $E_{\mathrm{T}}^{\mathrm{miss}}$ and τ triggers had 5-10% of the bandwidth each. This menu was deployed online in the end of 2010. To keep trigger rates within the required constraints one had to either raise p_{T} thresholds or tighten the trigger selection. This ever-changing menu brought unnecessary complication for physics analyses, and the trigger menus for the following years were designed to change as little as possible.

As all these peak luminosity values were at least an order of magnitude below the nominal low luminosity of LHC (10^{33} $\mathrm{cm^{-2}}$ $\mathrm{s^{-1}}$), the considerations behind the 2008 menu proposal (e.g. menu dominated by the low-p_{T} triggers with loosest selection possible) were very relevant to the ATLAS trigger menu strategy up to the end of 2010. Note that as the 2010 LHC run had a center-of-mass energy of 7 TeV (e.g. half of the nominal value of 14 TeV), trigger rates where roughly a factor of two less than the nominal ones which were considered in Table 3.4 and Table 3.5.

High-p_T objects in trigger

In the early 2010 I was appointed to coordinate trigger requests for the ATLAS Exotic analyses. The ATLAS Exotics Working Group is studying a wide variety of signatures to discover non-supersymmetric physics beyond the Standard Model. The group covers a wide variety of models, from Extra Dimensions and mini Black Holes to Dark Matter, exotics Higgs modes, Compositeness, etc. Given the wide scope of the physics signatures, the Exotics group takes interest in nearly all types of triggers in the menu, except the E_T^{miss} triggers which fall into the domain of the supersymmetry working group.

Considering the low thresholds and loose selections of the 2009-2010 ATLAS trigger menu, no dedicated exotics triggers were required. With major effort going into commissioning of the various systems, of particular importance to the Exotics group was ensuring good performance of the triggers for the very-high p_T objects, for which it is the main user.

First, the Exotics group wanted to ensure that no events are lost at L1, in particular for the calorimeter triggers. The extensive preparation work described below was done by the L1Calo experts. In order to assign the calorimeter tower signals to correct bunch-crossing, the signals must be synchronized to the LHC-clock phase with nanosecond precision. This was done with calorimeter pulser systems and cosmic-ray data and then refined with first beams. Special treatment, using additional bunch-crossing identification (BCID) logic, was needed for *saturated pulses* with E_T above about 250 GeV. The Run 1 BCID logic was verified for most trigger towers up to E_T of 3.5 TeV and beyond, which is of a huge importance to the analysis with high-p_T electrons, because if trigger mis-times those events are lost.

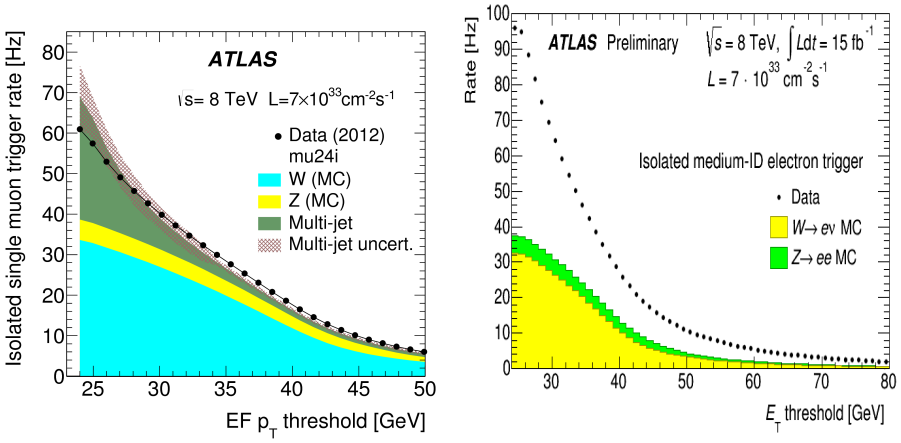

Figure 3.6: Single muon (left) and electron (right) trigger rate as a function of p_T(from [30, 31]).

The second concern was potential inefficiencies in the HLT reconstruction. As shown in Figure 3.6 most of the event rate for physics objects is concentrated at the lower range of the p_T-spectrum and often a contribution of the very high-p_T tail (above a few hundred GeV) to the rate is negligible. Thus the trigger menu usually contains dedicated high-p_T triggers with selections which are looser than for the corresponding low-p_T triggers to maximize their efficiency.

For example for the 2010 muon menu, the lowest trigger (mu13) was based on an algorithm which combined the inner detector and muon spectrometer tracks, but there was also a mu40_MSonly trigger which, as the name implies, was based on the muon spectrometer infor-

mation only. Using those two triggers in combination resulted in a few percent efficiency increase for the high-p_{T} muons, which is beneficial for the high-p_{T} exotics analyses.

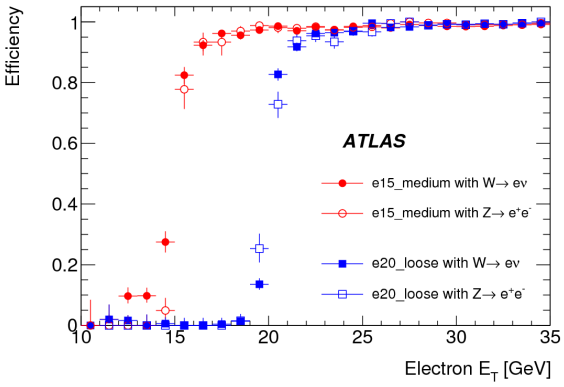

Figure 3.7: Efficiencies for the main single electron triggers, measured with respect to offline electrons in $Z \to ee$ events, shown as a function of ET in 2010. From [29, 31].

For electrons in addition to having looser electron triggers at higher thresholds (either with loose selection or with no selection at all in HLT, just an E_T cut) there was also a possibility to rely on the photon triggers. Those were deemed to be more robust, as they did not use the track reconstruction, which is the main source of the online/offline reconstruction differences. The Run 1 photon trigger selection was deliberately tuned to be looser than the corresponding offline electron one and the photon triggers also used electron calibration. In general in 2010, this duality was not crucial as the electron trigger efficiencies were extremely high, as can be seen in Figure 3.7.

For jet triggers, to avoid potential inefficiencies at the L2 jet reconstruction, for very-high-p_{T} objects there is a trigger which is based on the L1Calo selection only (L1_J95 in the 2010 menu).

Very high-p_{T} jets might not be fully contained within the calorimeters and 'punch-through' to the muon system, causing hits in the muon spectrometer. In this case the muon trigger reconstruction at HLT can reach the maximum allowed processing time exceeding 5 s at L2 and 180 s at EF (trigger time-out) and those events are then recorded in the *debug stream*. In the 2010 dijet resonant search analysis [32] the *debug stream* was found to contain 530 real jets, compared to 2.1 million jets reconstructed in the physics stream. In order not to bias the measured jet spectrum at high-p_{T}, these jets were included in the standard analysis and passed through the standard jet identification cuts. In general, to avoid any potential biases due to the trigger, all the ATLAS exotics analysis are required to study the events in the *debug stream*.

3.5.2 Renaissance: ATLAS Trigger Menu 2011 - 2012

The 2011 ATLAS trigger menu was designed over the winter shutdown aiming at a luminosity of $1-2\times10^{33}$ cm^{-2} s^{-1}. This menu had to be revisited once in the middle of 2011 for a luminosity of $3-5\times10^{33}$ cm^{-2} s^{-1} as the LHC performed beyond expectations. For the 2012 run the ATLAS trigger menu had to be updated again with a target peak luminosity of 8×10^{33} cm^{-2} s^{-1}. These menu changes were forced by the limited number of the L1 thresholds in Run 1 (shown in Table 3.2), which did not allow the trigger menu to accommodate a wider luminosity range.

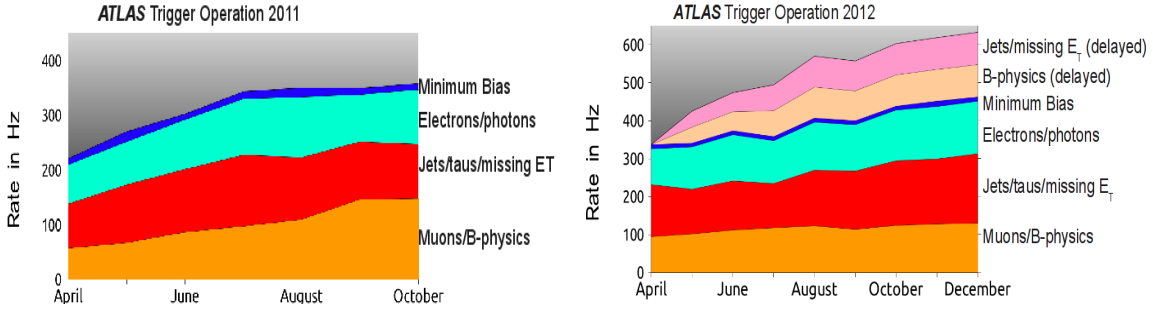

Figure 3.8: Event Filter stream recording rates per month, averaged over the periods for which the LHC declared stable beams for 2011 (left) and 2012 (right) [33].

In Run 1 there were four primary physics streams: *Egamma, Muons/B-physics, JetTauEtmiss and Minbias*. Their rates are shown in Figure 3.8.

Following extensive discussion in the physics analysis groups in the end of 2010, priority in the trigger menu was given to the most generic triggers, e.g. single electron and single muon with threshold of 20-25 GeV. They were allocated the largest bandwidth at all levels, with a typical EF output rate of around 50 Hz or more each. As most of the trigger thresholds for single object triggers had to increase with respect to 2010, there was a tendency to introduce more multi-purpose multi-object triggers which allowed to keep p_{T}-thresholds reasonably low. For example if the main single muon trigger was mu18, the dimuon trigger was 2mu10 and the tri-muon trigger was 3mu4. These triggers typically had 5-15 Hz of output bandwidth.

The main challenge to the trigger in this period was the increase in the number of collisions per beam crossing (pile-up) from on average 2 in 2010, to 9 in 2011 and to 23 in 2012. This required multiple changes to the trigger chain configurations to reduce their pile-up dependence and led to the raising of some thresholds in the trigger menu.

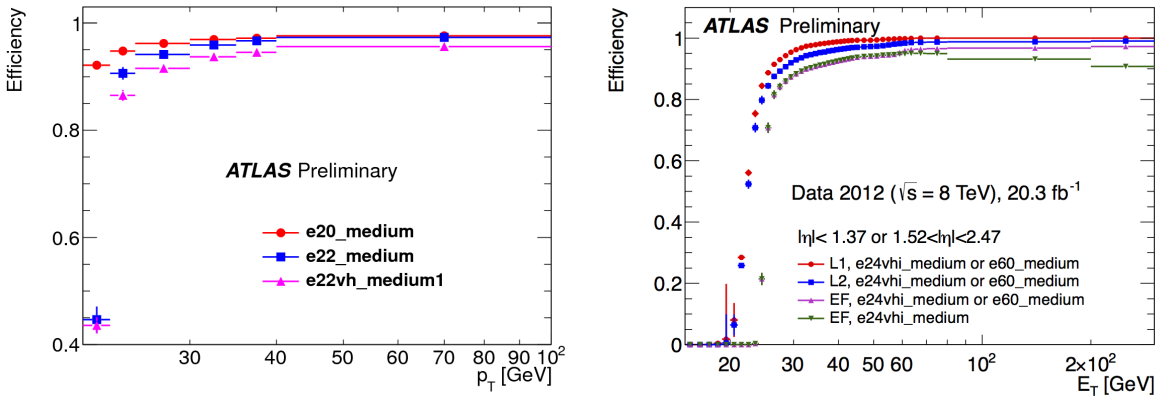

Figure 3.9: Efficiencies for the main single electron triggers, measured with respect to offline electrons in $Z \rightarrow ee$ events, shown as a function of E_{T} for (left) 2011 and (right) 2012 data. From [31]. Note the different vertical scales of the figures.

These developments can be seen clearly in an example of the single electron triggers. The energy dependence of the efficiencies of the lowest unprescaled single electron triggers used in 2011 and 2012 is shown in Figure 3.9. It can be seen that the trigger efficiency with respect

to online became progressively worse as the online selection becomes tighter. Those efficiency losses have a few different sources. The L1 energy resolution contributes significantly close to the E_{T} threshold, particularly after introduction of the L1 hadronic veto and E_{T} threshold-η-dependence later in 2011 (e.g. in e22vh_medium). The other source of inefficiency in the whole p_{T}-range comes from the HLT tracking selections (both fast and precision). In particular, the online tracking for electrons does not use the Gaussian Sum Filter, which was introduced in the offline in 2012. This effect can be seen as inefficiency in both L2 and EF in Figure 3.9 (right). The same figure also shows inefficiency at high-p_{T} caused by introduction of the electron isolation. The latter effect was mitigated by combining a low-p_{T} isolated electron trigger with a higher-p_{T} non-isolated electron trigger (e.g. e60_medium).

Dedicated exotics triggers

Multi-purpose triggers, discussed above, did not work well for some exotics analysis, in particular because standard object identification was not efficient enough and very analysis-specific triggers had to be introduced. Those triggers were allocated about 1 Hz of the EF rate and therefore needed quite sophisticated trigger selections.

One example is a dedicated trigger for heavily ionizing particles, such as monopoles, which could either rely on a single photon trigger (e.g. g120_loose) or develop a dedicated trigger with a requirement on a very high fraction of high-threshold hits in TRT based on L1_EM20. This dedicated trigger allowed ATLAS to increase considerably the acceptance for the high charge monopoles [31].

Another example is triggers for the long-lived-particles whose decay products would be displaced from the interaction point. Most of standard object reconstruction (in particular involving tracking) requires particles to come from the interaction region and thus would not work for those final states. Two exceptions are a muon-spectrometer-only reconstruction for muons and a photon reconstruction applied for either electron or non-converted photon final states. For models with high-p_{T} objects of this kind single object general-purpose triggers could be used. Dedicated triggers were introduced to cover the lower part of the p_{T}-spectrum (2mu10_MSonly_g10_loose and 3mu6_MSonly).

In addition to the above, three dedicated types of triggers were introduced in the trigger menu to record candidate events for long-lived particles decaying in different parts of the detector [34]. Triggers for objects decaying in the inner detector and electromagnetic calorimeter are characterized by presence of jets with no tracks from the interaction region. Triggers for objects decaying in the muon spectrometer are characterized by presence of muons with no tracks from the interaction region. Triggers for objects decaying in the hadronic calorimeter are expected to have a hadronic cluster without an electromagnetic one present. In addition to the main analysis triggers outlined above, there was also a set of equivalent triggers in non-collision bunches for background studies.

Last but not least are the so-called *fat jet triggers* with anti-k$_T$ jets with R=1.0 reconstructed at the event filter. This trigger was originally developed for the boosted $t\bar{t}$ resonant exotics searches in a fully hadronic channel, but quickly became part of the general-purpose jet menu.

Jet menu and new phenomena searches in the dijet channel

The jet trigger menu constituted approximately 10% of the bandwidth in Run 1. It consisted of single central and forward jet triggers, a set of unprescaled multi-jet triggers and all the lower

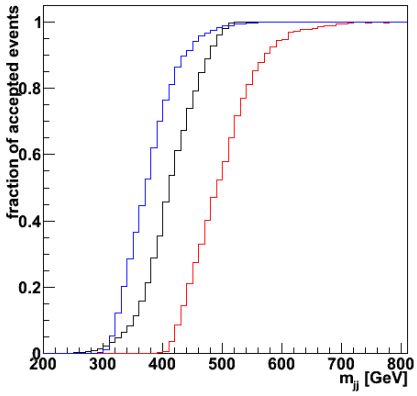

Figure 3.10: Toy study of expected single jet and dijet trigger efficiencies for the dijet mass search [35]. The black curve corresponds to a 200 GeV leading jet and reaches 99% efficiency at 500 GeV. The red curve corresponds to two 200 GeV jets and is efficient at 800 GeV. The blue curve corresponds to two 150 GeV jets and is efficient at 500 GeV but leads to higher expected rate.

threshold triggers prescaled to a fixed rate (below-Hz-level).

In the end of 2010 [29] the lowest unprescaled jet threshold was L1_J95 and multi-jet triggers started from a prescaled EF_2j75 trigger. With jet bandwidth being at a premium, I was involved in a discussion on the usefulness of the dijet triggers. A toy study summarized in Figure 3.10 was performed by F. Ruehr [35] to address this issue. It showed that using a symmetric dijet trigger is equivalent to using a single jet trigger with twice the threshold, at a cost of at least 70% more trigger rate. Also while it could be possible to develop asymmetric triggers at the same rate, the potential gain of signal acceptance was found to be only 10% and very analysis-specific. On the basis of this study, it was decided to drop dijet triggers from the trigger menu.

A permanent concern of the exotics analyses involving jets, was the ever increasing threshold of the unprescaled single jet trigger which was limited to a fixed unique rate of 10 Hz. With luminosity projected to raise constantly this meant that once a jet trigger threshold became prescaled (usually to about 0.5 Hz flat rate), the data accumulated by that particular jet threshold did not scale with luminosity any more, but rather increased linearly with time, making it of marginal interest for searches.

In 2010 the unprescaled jet threshold was L1_J95 and in 2011 it was set to increase to at least j180 (an anti-k$_T$ topo-cluster jet of E_{T}=180 GeV with R=0.4 reconstructed with full-scan algorithm at the EF). To maintain our sensitivity to low-cross-section new phenomena in the lower dijet mass range it was decided to use a prescaled trigger (j135), with a prescale of not higher than 10, giving it 3-5 Hz rate. This allowed the integrated luminosity for j135 to scale with the LHC luminosity increase.

A new feature introduced in 2012 was the so-called *delayed streaming*. It used spare output capacity in the DAQ system to record an additional 100 Hz of lower p_{T} jet triggers (unprescaled j220 versus j360 in the standard streaming) for reconstruction when spare offline processing power became available (e.g. potentially weeks or month after the data was recorded). Dijet events from the delayed data stream fall primarily into the region between 750 GeV and 1 TeV. The delayed stream increased the luminosity recorded in this region of phase space by up to an order of magnitude as is shown in Figure 3.11.

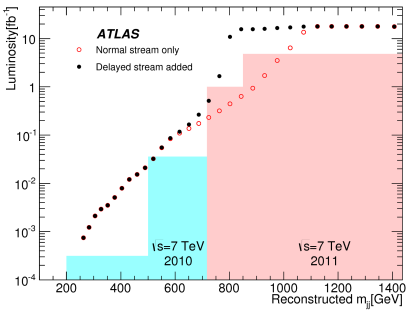

Figure 3.11: Recorded effective integrated luminosity as a function of dijet mass for all former ATLAS dijet searches (shaded boxes). The integrated luminosity per dijet mass bin from the 2012 data used in the current analysis is shown without (open circles) and with (filled circles) the added delayed data stream from Ref. [36].

These jet trigger menu adaptations allowed to fully explore the dijet mass below that covered by lowest unprescaled single jet trigger in Run 1. A new approach adapted in Run 2 is discussed in Section 3.6.

3.6 Industrial Revolution 2013-2014: ATLAS Run 2 Trigger

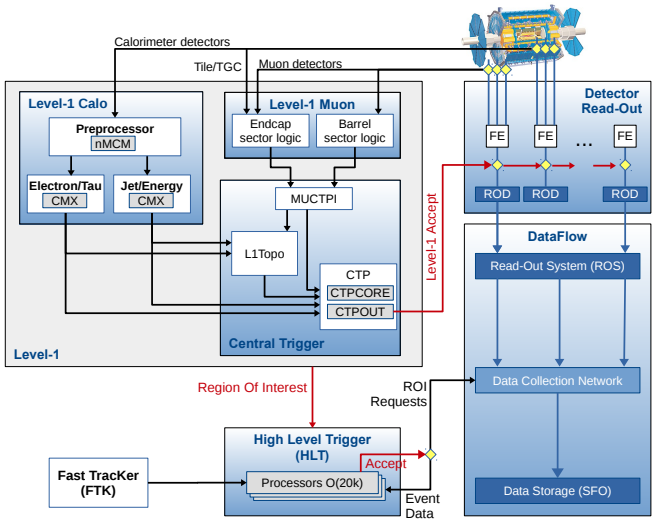

Figure 3.12: The ATLAS Trigger/DAQ system in Run-2 with emphasis on the components relevant for triggering. Additional software and hardware components used in the data flow implementation are not shown.

In 2013 I was appointed as one of two Trigger Menu Coordinators. My main charge was to develop the trigger menu for the Run 2 data-taking.

There were many important changes and additions to the existing trigger and DAQ system during LS1 (2013-2014). They enabled us to maintain the Run 1 physics sensitivity despite a five-fold increase in the trigger rate in Run 2. A schematic view of the current TDAQ system is shown in Fig. 3.12.

3.6.1 L1 trigger updates during LS1

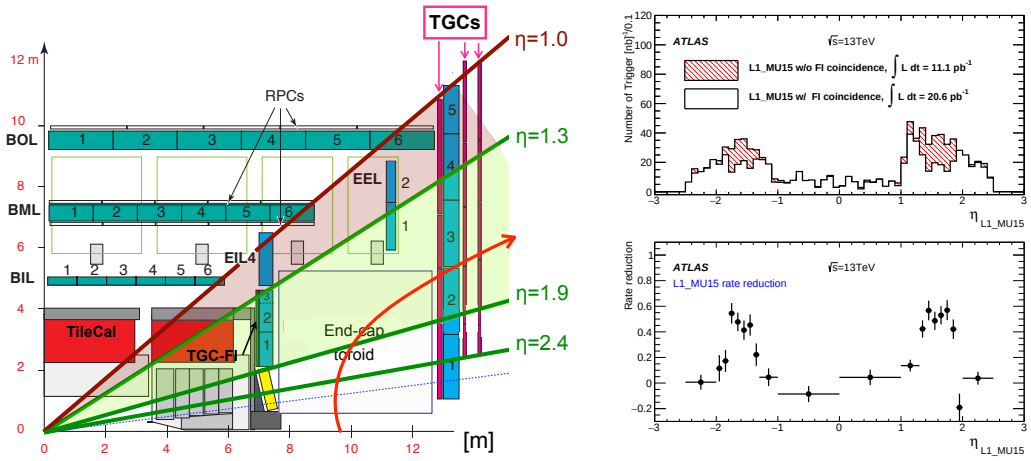

Figure 3.13: (left) A schematic view of the ATLAS Muon spectrometer with lines indicating various pseudo-rapidity regions. The red curved arrow shows an example of a trigger due to slow particles generated at the beam pipe around $z \sim 10\,\text{m}$. (top right) Distributions of RoIs from the L1_MU15 trigger. The number of the entries is normalized to the integrated luminosities in the runs with and without the FI coincidence enabled. (bottom right) Rate gain due to TGC-FI coincidence.

The L1Muon system shown in Figure 3.13 (left) underwent various upgrades in order to reduce the trigger rates in the endcap region and to increase the acceptance in the barrel region. During Run 1, only TGC chambers furthest from the interaction point were used to generate triggers. A new trigger logic was introduced for Run 2 requiring an additional coincidence with the Inner layer of the TGC chamber (TGC-FI) in the $1.0 < |\eta| < 1.9$ region and with the outer-layer of the Tile calorimeter in the $1.0 < |\eta| < 1.3$ region. The former coincidence was deployed and validated during the 2015 run and shows up to 60% trigger rate reduction in the relevant region as shown in Figure 3.13 (right). The latter coincidence is still under commissioning. Further rate reduction could be achieved by a masking of localized high rate regions. Some RPC chambers installed in the feet and elevator region in the bottom part of the detector, which were non-functional during Run 1, were equipped with the trigger electronics during LS1 and are currently undergoing commissioning. They are expected to increase the trigger acceptance for high-p_{T} muons by about 3%.

During LS1, a number of upgrades were made to the L1Calo electronics components. New FPGA-based multi-chip modules (nMCMs) were produced and replaced the old ASIC-based MCMs in the PreProcessor system. This new hardware allows the use of auto-correlation filters

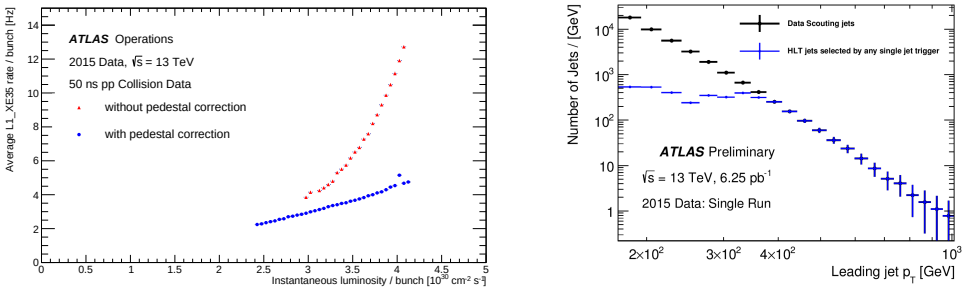

Figure 3.14: (left) The trigger rate for the missing E_{T} trigger with a threshold at 35 GeV as a function of the instantaneous luminosity per bunch. The rates are shown for different settings with and without pedestal correction applied. The pedestal correction minimizes pile-up effects and linearizes the trigger rate. (right) Distribution of the transverse momentum of leading HLT jets recorded in the *Trigger-Level-Analysis jet stream* (triggered by the unprescaled L1_J75 trigger), marked as Data Scouting jets (in black), compared to the distribution of all leading HLT recorded by any of the single jet high level triggers in the main physics stream in a single run (in blue).

and a new bunch-by-bunch dynamic pedestal correction, meant to suppress pile-up effects. The effect of these corrections in linearizing the L1 multi-jet and $E_{\mathrm{T}}^{\mathrm{miss}}$ trigger rates as a function of the instantaneous luminosity is shown in Figure 3.14 (left).

One unexpected effect of this update was mis-timing of the saturated L1Calo triggers (e.g. triggers for electrons, taus, photon or jet objects with p_{T}>1.8 TeV) by one bunch-crossing too early due to the presence of negative autocorrelation coefficients. All saturated events regardless timing had been saved to a dedicated stream. In total 122 events were found to be mistimed in the 3.2 fb^{-1} of data of the 2015 25 ns proton-proton run. Those events were reprocessed and reintegrated into all relevant physics analyses except the analyses with high-p_{T} electrons, as there was no tracking information present in those events. This issue is expected to be resolved in 2016 L1Calo firmware updates.

The updated Cluster processor firmware included implementation of five new E_T-dependent isolation thresholds each for EM and TAU and doubled the number of the L1Calo thresholds per type as shown in Table 3.2. The increase in the number of thresholds allows to accomodate more L1 triggers in the trigger menu, covering the full expected luminosity range of the Run 2. The E_T-dependent isolation provides better control of the L1 trigger rates. These changes give a higher flexibility in the Run 2 trigger menu planning.

The new L1Calo merger modules no longer output hit counts for e/γ, τ and jet. They provide, instead, trigger objects (TOB), which comprise the location, energy, isolation bit, type of object identified as well as total transverse energy (TE), missing transverse energy (XE) and missing transverse energy significance (XS) triggers.

Information of TOBs above a certain threshold is sent to the new L1 topological trigger processor (L1Topo), which also receives data from L1Muon via the MUCTPI. L1Topo consists of two or more FPGA-based processors which can be programmed to perform selections based on the geometrical relationship between trigger objects received from L1Calo or L1Muon (e.g. angular selection, invariant mass, or global event quantities such as the sum of the transverse momenta of all L1 jet objects). The system was fully installed in 2015 and is currently being

commissioned.

The upgraded CTP will provide more trigger inputs, making room for new trigger sources (e.g. topological processor), as well as more L1 trigger menu items (512 instead of 256) and bunch groups (16 instead of 8).

3.6.2 HLT updates during LS1

The previous two-level HLT farm consisting of L2 and EF were merged into a single homogeneous farm allowing for better resource sharing and overall simplification both on the hardware and software side.

Most of the trigger reconstruction algorithms were re-optimized to minimize differences between the HLT and the offline analysis selections, which in some cases, such as in the hadronic tau triggers, reduced inefficiencies by more than a factor two.

A baseline average HLT output rate for Run 2 has been increased to 1 kHz due to sufficient storage and CPU resources being available. To minimize event duplication from having multiple inclusive physics streams it was decided to record physics events into a single stream called *Main*. This reduces the event overlap and thus storage and CPU resources during reconstruction by roughly 10%.

Another improvement in Run 2 is an adaptation of the *partial event building* technique to record only HLT objects. As with other calibration streams this results in a very small event sizes, thus enabling very high recording rates. This feature was used in 2015 to record events for the dijet search analysis. Recording all the events triggered by the L1_J75 trigger in the *Trigger-Level-Analysis jet stream*, the maximum rate of data recorded to disk was 1.1 kHz, for an event size of roughly 3 kB per event (while the size of the *Main* physics stream is around 800 kB per event). As the performance of jets reconstructed at the trigger level is comparable to that of jets reconstructed offline, this data will allow to achieve significant improvements in the sensitivity of searches for light resonances decaying to jets, as is shown in Figure 3.14 (right). It will allow ATLAS to permanently resolve the issue of an ever increasing threshold for unprescaled single jet triggers discussed in Section 3.5.2.

3.7 Modern Times: ATLAS Run 2 Menu 2015

Despite the $2-2.5$ times higher expected trigger rates due to the increased center-of-mass energy from 8 to 13 TeV, the main goal of the Run-2 trigger menu design was to maintain the single unprescaled electron and muon triggers around 25 GeV. This approach, based on inclusive triggers aimed at the widest possible variety of physics processes (including W and Z boson decays), allows for the optimal use of the bandwidth and minimizes the need for additional support triggers.

The Run-2 trigger menu has been designed for an ultimate luminosity of $2{\times}10^{34}$ cm^{-2} s^{-1}, which included an extra margin due to uncertainties in the trigger rates extrapolations. The adjustments to the trigger thresholds are planned in luminosity steps of $0.5{\times}10^{34}$ cm^{-2} s^{-1} but triggers at higher luminosities are always included at the lower luminosity points. This approach was made possible by the increase in the number of the L1 items and L1Calo thresholds. It simplifies analyses using the same trigger for the full Run-2 dataset while allowing other analyses to choose the lowest available trigger threshold at any given time.

3.7.1 2015 Start-up Menus

The first LHC stable beam collisions at 13 TeV occurred in the morning of June 3, 2015. For the first week of data-taking in 2015, the LHC planned special machine configuration with only a few (2 or 8) bunches or one train of 6 bunches circulating in the machine. With the expected luminosities of 1–10$\times10^{31}$ cm^{-2} s^{-1}, the total HLT rate for even the lowest 2015 physics menu point was expected to be only a few tens of Hz and for the L1 menu 200-2000 Hz. It was decided for the first two weeks of the data-taking that we could afford to record up to 2 kHz of the average HLT output rate.

The ATLAS trigger system was commissioned extensively before the 2015 LHC beams with similar procedures as described in Ref. [29], but to ensure extra-safe data-taking HLT algorithms were not enabled online for the very first collisions. A special trigger menu was created which selected the events based solely on their L1 decision, completely bypassing HLT. This trigger was based on the 5×10^{33} cm^{-2} s^{-1} L1 menu and a few complementary L1 items with lower thresholds to increase the final event statistics. This data was used for the ATLAS detector and trigger commissioning. For example, the 2015 physics menu was rerun offline on those events to ensure correct functioning of all HLT algorithms.

Those first runs also had some special requests which required enabling a limited set of the HLT triggers, in particular single electron and muon triggers (for TRT gas study at different voltages), single and forward-central jet triggers for the jet $\eta - \phi$ inter-calibration and a single photon trigger for the SM studies. Those triggers were enabled online one by one and kept enabled until collected the required number of events.

The following week of June 8th (Week 2) was dedicated to special fills with low beam currents and reduced focusing (e.g. average pile-up per bunch crossing varied between 0.003–0.03). This was a unique opportunity to collect minimum bias events for QCD studies and high-track-multiplicity (ridge) analysis at 13 TeV (although similar runs were taken in Run 1 at lower center-of-mass energies). The menu for this run was based on Minimum Bias Trigger Scintillator triggers (MBTS), which consist of two planes of twelve counters sensitive to charged particles in the interval $2.07 < |\eta| < 3.86$. In addition, an ultra-forward trigger was provided by the LHCf experiment.

In the end of Week 2, LHC reverted to the standard beam configuration and in the stable collisions of 6 trains of 6 bunches on June 13th full 2015 physics menu was run online successfully for the first time.

As I stepped down as a menu coordinator in the end of June 2015, this start-up period was the only part of the 2015 data-taking I have personally participated in. In June 2015 ATLAS has recorded 8 pb^{-1} of data at the nominal beam settings and over 200 million soft interactions.

3.7.2 2015 Physics Menu

Table 3.7 shows a comparison of selected primary trigger thresholds used during Run 1 and 2015. Although there are a few threshold increases (the L1 threshold for single electrons), there are also some lower thresholds (HLT $E_{\mathrm{T}}^{\mathrm{miss}}$ triggers and single muons) and looser selections (non-isolated single electrons at HLT), which lead to either better efficiencies or better phase-space coverage for many ATLAS analyses. It should be also noted that for runs taken at the peak luminosity in 2015, average HLT rate exceeded its 1 kHz budget and was ∼1.2 kHz.

Although LHC center-of-mass energy increased from 8 to 13 TeV, the 2015 peak luminosity was actually a bit lower than in 2012 (5.2×10^{33} cm^{-2} s^{-1} vs 7.7×10^{33} cm^{-2} s^{-1}) leading to an

Table 3.7: Evolution of the trigger menu. The total rate corresponds to the full menu that includes many more triggers than what is listed in this table. Electron and τ identification is assumed to be of 'medium' flavor, unless specified otherwise. Photon and b-jet identification is assumed to be of 'loose' flavor. Trigger isolation is denoted by "i".

Year	2012		2015		2016	
$\sqrt{s}$ [TeV]	8		13		13	
Peak Luminosity	7.7×10^{33} cm^{-2} s^{-1}		5.0×10^{33} cm^{-2} s^{-1}		15×10^{33} cm^{-2} s^{-1}	
Category	p_{T} threshold [GeV], selection					
	L1	HLT	L1	HLT	L1	HLT
Single electron	18	24i	20	24	22i	26i,tight
Single muon	15	24i	15	20i	20	26i
Single photon	20	120	20	120	22	140
Single τ	40	115	60	80	60	160
Single jet	75	360	100	360	100	400
Single fat jet	75	360	100	360	L1Topo	460
Single b-jet	n/a	n/a	100	225	100	300
$E_{\mathrm{T}}^{\mathrm{miss}}$	40	80	50	70	50	70
Dielectron	2×10	2×12,loose	2×10	2×12,loose	2×15	2×17,loose
Dimuon	2×10	2×13	2×10	2×10	2×10	2×14
Electron,muon	10, 6	12, 8	15, 10	17, 14	15, 10	17, 14
Diphoton	16, 12	35,25	2×15	35,25	2×15	35,25,medium
Ditau	15, 11i	27, 18	20, 12	35,25	L1Topo	35, 25
Electron,tau	14, 11i	18, 28i	15, 12(+jets)	17i, 25	L1Topo	17, 25
Muon, tau	10, 8	15, 20	10, 12(+jets)	14i, 25	L1Topo	14, 25
Four jets	4×15	4×80	3×40	4×85	3×50	4×100
Six jets	4×15	6×45	4×15	6×45	4×20	$6\times50(\lvert\eta\rvert<2.4)$
Peak L1 rate (kHz)	65		70		100	
Average HLT rate (Hz)	400		1200		1000	

expected average increase of the trigger rates of about 35%. This rate increase is comfortably accommodated by the increases in the allowed L1 and HLT rates of about 45% and 250% respectively. There was also less pile-up as for the major part of 2015 LHC was running with 25 ns bunch-spacing.

Typical distribution of bandwidth among various object types is shown in Figure 3.15(left). One would expect it to be dominated by single electron and muon triggers, but actually the dominant contributions are $E_{\mathrm{T}}^{\mathrm{miss}}$, electron and b-jet triggers. As time for the trigger commissioning in 2015 was expected to be very limited, $E_{\mathrm{T}}^{\mathrm{miss}}$, electron and b-jet triggers based on the experimental algorithms or more robust object selection (e.g. with some variables removed, different taggers) were implemented in the menu in addition to the standard ones as described in Ref. [37]. This proliferation of triggers results in a higher-than-usual rate contributions of those signatures. Unique rate of the support triggers is approximately 20%. Figure 3.15 (right) shows typical stream rates at the HLT as a function of instantaneous luminosity. Representative L1 trigger rates are shown in Figure 3.16.

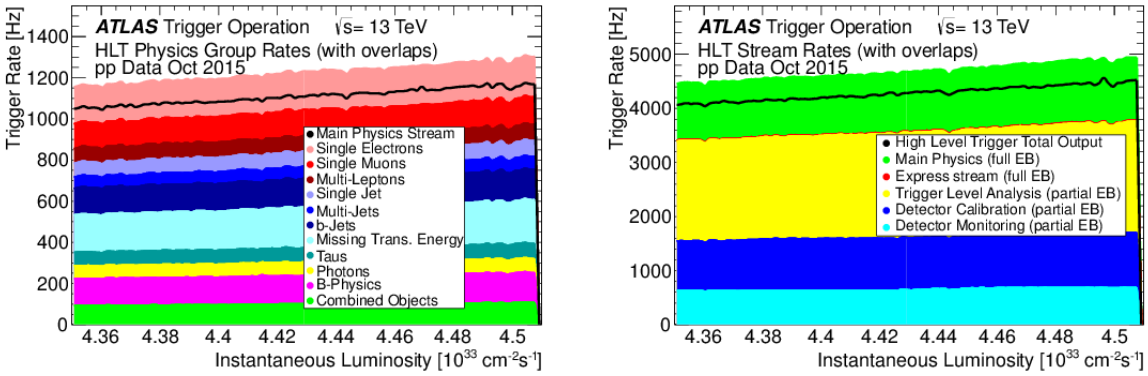

Figure 3.15: (left) HLT rates of the specific for trigger physics objects as a function of the instantaneous luminosity (for illustration purposes). As all those events are recorded in the Main stream overlaps are accounted for in the total output rate. (right) Total and individual stream rates at the HLT as a function of the instantaneous luminosity. Stream overlaps are accounted for in the total in the total output rate. The steps in the rates reflects changes in the trigger menu composition, achieved via changes in prescales. Data comes from a fill taken in October 2015 with a peak luminosity of 4.6×10^{33} cm^{-2} s^{-1} and an average pile up of 15.

One of the main operational constraints in 2015 was the L1Accept rate limitation coming from the IBL fixed frequency veto (FFTV). If time varying currents are passed through them in a magnetic field, mechanical resonances can lead to the breaking of bond wires. FFTV are designed to minimize the dangers of breaking wire bonds, by avoiding data taking at the same BCIDs: occupancy in bins of BCID should remain below 40%. The value of the L1 rate limitation is dependent on the number of the LHC bunches and how they are distributed at the LHC. Constrains are strongest at small numbers of bunches, e.g. during first runs with 2 bunches we were limited to about 4kHz. But even at 1000 bunches the rate limit is only around 50 kHz and it reaches 100 kHz only at 1800 bunches. This constraint had to be taken into account in the 2015 trigger operations when the menu prescale set for a particular LHC configuration was chosen. This constraint might be even stronger in 2016 if the LHC beams are more focused (e.g.

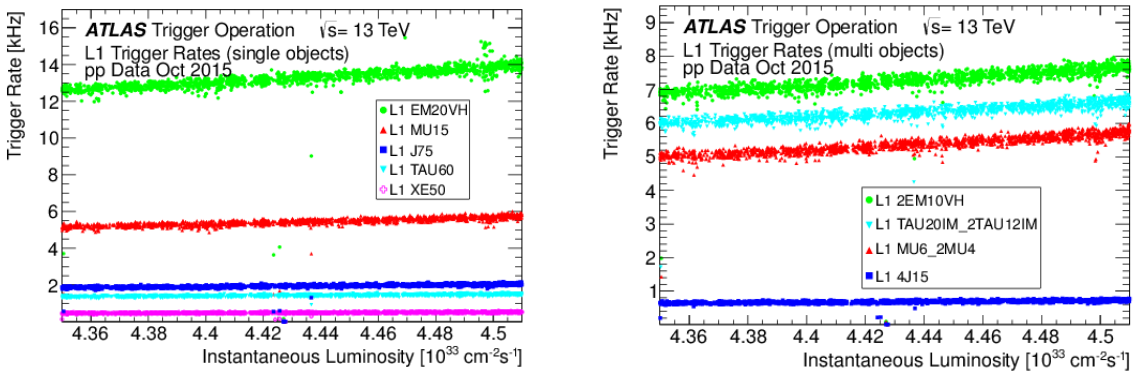

Figure 3.16: Representative first level trigger rates as a function of luminosity for (left) single object triggers and (right) multi-object triggers.

$\beta^* = 40\,\text{cm}$ instead of 80 cm in 2015), allowing to reach the same luminosities at half of the number of bunches.

More information about the performance of the ATLAS Trigger System in 2015 can be found in Ref. [37].

Table 3.7 also shows the expected primary triggers for the Run-2 menus beyond 2015. Although some thresholds (e.g. single and dielectrons) have to be adjusted at higher luminosities, most of the trigger menu is expected to stay stable up to the end of Run 2. Note that there are a few items marked with 'L1Topo' in the table, which rely on the use of L1Topo to maintain the trigger thresholds at the current values (e.g. relevant for $H \to \tau\tau$).

3.8 Conclusions

The ATLAS trigger system has operated successfully during the 2009−2012 and 2015 runs of the LHC. The ATLAS trigger menu, based on single electron and muon triggers around 25 GeV, provided the efficient coverage to the all physics processes of interest to the ATLAS physics program. The rapidly rising luminosity and pileup conditions at time have been a challenge to the trigger. It needed to evolve many of its selections many times to keep both high efficiency for the most interesting physics channels and within the available bandwidth. These challenges have been met and significant improvements both implemented during LS1 and still in the pipe-line, such as Fast TracKer, should enable the ATLAS trigger system to easily face the increasing luminosity of the Run 2. ATLAS Trigger Menu which I have developed was used successfully in 2015 and should work with some minor modifications until the end of the Run 2.

3.9 My contributions

- 2007-2010 I worked in Electron and photon performance group as a trigger menu contact person. I developed triggers for the J/ψ tag-and-probe electron efficiency determination. I also was a member of Trigger Menu Coordination Group and worked on the electron trigger menu.

- 2010-2012 I was a trigger menu contact person for the ATLAS Exotics working group and a member of Trigger Menu Coordination Group, responsible that all the signal, background and support triggers for the Exotics group analyses are implemented in the trigger menu. This responsibility required to coordinate with all exotics analysis teams their trigger strategies for the future data-taking. With over a 100 papers for the ATLAS Exotics working group in Run 1, I believe my effort was successful.

- 2013-2015 I was one of two ATLAS trigger menu and signature group coordinators, responsible for the Run 2 trigger menu design and commissioning. This trigger menu defines the scope of the Run 2 physics program for the ATLAS experiment. As menu coordinator I was charing weekly Trigger Menu General meetings, monthly Menu Coordination Group meetings and Signature Coordination Group meetings. I was also member of ATLAS Physics Coordination Group and ATLAS Trigger Coordination group.

- 2011-2016 I took *online trigger shifts*, in which shifter has to ensure that the correct trigger menu prescale set is used for the data-taking and does first basic check on the trigger data quality variables. I also took offline trigger shifts (called Data Quality expert shifts since the start of Run 2), in which the shifter checks of the trigger data quality variables using express stream events and studies the debug stream events.

Chapter 4

Physics Analysis

4.1 Introduction

In 2008-2009, at the time of the LHC start-up, the expectations ran high that some kind of new physics would be discovered immediately. But the type of that new physics was unknown and thus model-independent generic searches were required. Basically everyone had to choose the final state they liked and "opened the box" to see if they got the jackpot. But which channel to work on?

My earlier career and, in particular, my interest in electromagnetic calorimetry brought me to focus on the final states with electrons. Since joining the ATLAS experiment as a CERN fellow in 2006, I have worked on electron reconstruction, performance and triggers. Moving to LAPP in 2008 only strengthened that interest as the LAPP-ATLAS group has been involved in the design, commissioning and operation of the ATLAS electromagnetic calorimeter (used for electron reconstruction and identification). For high-p_{T} searches electrons are attractive as their resolution improves with p_{T}.

The next question was: how many? In this area, I was also not too adventurous and decided to stay with a final state of two, which I already studied with J/ψ decays both for my thesis on the BaBar experiment [38] and for my trigger work at ATLAS [39]. The other attraction was that the dilepton (dielectron and dimuon) final state has a long and illustrious history with the discovery of the J/ψ meson in 1974 [40, 41] and Υ meson in 1977 [42] as well as the direct observation of the Z boson in 1983 [5, 6]. As these were key steps which led to the establishment of the SM, maybe the same final state could help to enlighten us on the physics processes beyond it.

One of the advantages of this final state is that various models have resonances decaying to dileptons: a spin-0 particle could correspond to a sneutrino in R-parity violating supersymmetric models [43], a spin-1 could be a new gauge boson of a Grand Unified Theory (Z') [44] and a spin-2 resonance could be identified as a Kaluza-Klein excited graviton in the Randall-Sundrum model [45].

In experimental terms all these will result in a "bump" on top of a smoothly falling dilepton mass spectrum and thus this search is model-independent. Also this final state is fully-reconstructable with small and well-understood backgrounds, which makes it one of the most attractive search channels in the busy environment of the LHC. Thus dielectrons were (and are for the moment) my final state of choice.

A typical benchmark model for the dilepton search is the Sequential Standard Model (SSM) [44], where Z'_{SSM} has the same couplings to fermions as the Z boson and a width of approximately 3% of its mass. The decays into dibosons, which would otherwise be dominant, are suppressed.

Previous searches have set direct and indirect constraints on the mass of the Z'_{SSM} resonances. The Tevatron experiments excluded a Z'_{SSM} with masses lower than 1.07 TeV [46, 47]. Indirect constraints from LEP [48, 49, 50, 51] extend these limits to 1.79 TeV.

The ATLAS dilepton analysis focused on narrow resonance searches in the mass range above the Z boson mass (e.g. from $\sim$ 120 GeV). Although the mass range below 1 TeV has already been excluded for the Z'_{SSM} benchmark model, there could still be some new physics processes with smaller cross-sections, which have not been detected yet.

Every major step in the LHC energy and the integrated-luminosity increase led to a major improvement in the signal sensitivity and thus resulted in a publication. Four papers were published by ATLAS: three at the center-of-mass energy of 7 TeV with 40 pb^{-1} [52], 1.8/2.1 fb^{-1} [53] and the final dataset of 4.9 fb^{-1} [54] and one at the center-of-mass energy of 8 TeV [25]. The fifth paper with 3.2 fb^{-1} at the center-of-mass energy of 13 TeV is currently in preparation. The CMS collaboration also has a similar set of publications, of which I will consider only the latest one at the center-of-mass energy of 8 TeV in this manuscript [55].

4.2 Searches for new resonant phenomena in dilepton mass spectrum

4.2.1 Data Sample

The discussion in this manuscript focuses on the results based on about 20 fb^{-1} of proton-proton LHC collision data collected in 2012 at the center-of-mass energy of 8 TeV[25]. The events were collected during stable beam periods and all relevant systems operational.

In the dielectron channel, events are triggered by g35_loose_g25_loose trigger. It has looser trigger selection requirements compaired to either di-electron or single electron triggers, which facilitates estimation of the data-driven backgrounds in the electron channel.

In the dimuon channel events are triggered by the mu24i and mu36 triggers. Note the absence of the MS-only muon trigger requirement: although its usage might have resulted in a few % higher signal efficiencies in the muon channel, it was overlooked as it was not part of the official muon trigger group recommendations in 2012.

4.2.2 Simulated Samples

Expected signal and background yields, with the exception of a data-driven estimate for the *Dijet and W+jet* background[1], are evaluated with simulated Monte Carlo (MC) samples and normalized to the highest-order cross-section predictions available in perturbation theory. The details of the simulated signal and background samples are given in Ref. [25].

The main background in this analysis is the Drell-Yan process ($q\bar{q} \rightarrow Z/\gamma^* \rightarrow l^+l^-$). For this background the cross-section as a function of dilepton mass has been calculated consistently (for the first time) for both the exotics group analysis and the Drell-Yan double-differential

[1]This background comes from events with jets or photons in the final state that pass the electron selection criteria)

cross-section measurement[2] at next-to-next-to-leading order perturbative QCD with FEWZ. This calculation included next-to-leading order *EW corrections* beyond final state radiation, as well as contribution from the irreducible non-resonant Photon-Induced background (*PI correction*), and a small correction arising from single boson production with final state lepton radiating from a real W or Z boson.

Other important backgrounds are due to diboson (*WW, WZ* and *ZZ*) and top quark production. The simulated top samples were statistically limited at high invariant mass and the expected number of events as a function of m_{ll} is therefore extrapolated into this region using fits.

Templates for the signal models are obtained by re-weighting Drell-Yan signal samples to the model-dependent shape of the resonance as detailed in Ref. [56]. As the width of the resonances considered is small, we assume that interference effects can be ignored.

Event selection

Events are required to have at least one reconstructed primary vertex and at least two lepton candidates of the same type passing all selection criteria. Electron and muon object reconstruction was described in Section 2.3.

This analysis uses *medium* electrons identification criteria. To further suppress background from mis-identified jets, only isolated electrons are selected. The isolation value was optimized to maintain high efficiency for each electron candidate. The energy, corrected for transverse shower leakage and underlying event, contained in a cone of radius $\Delta R = 0.2$ surrounding the electron candidate is required to be less than $0.007(0.022) \times E_{\mathrm{T}} + 5.0(6.0)$ GeV for the leading (sub-leading) electrons. The leading (subleading) electron must satisfy $E_{\mathrm{T}} > 40(30)$ GeV. The transition region between the central and endcap regions of the calorimeters, in the range $1.37 \leq |\eta| \leq 1.52$ is excluded. The calorimeter resolution for electrons above ∼200 GeV is 1.2% in the central region ($|\eta| < 1.37$) and 1.8% in the forward region ($1.52 < |\eta| \leq 2.47$).

Muon candidates are reconstructed with the high p_{T} muon selection [25]. To reduce the background from mis-identified jets, each muon is required to be isolated such that $\sum p_T(\Delta R < 0.3)/p_T(\mu) < 0.05$, where $\sum p_T(\Delta R < 0.3)$ is the scalar sum of the p_{T} of all other tracks with $p_{\mathrm{T}} > 1$ GeV within a cone of radius $\Delta R = 0.3$ around the direction of the muon. Muons passing the reconstruction criteria are required to have $p_{\mathrm{T}} > 25$ GeV and have opposite sign. The p_{T} resolution of muons at 1 TeV ranges from 19% to 32%, depending on η.

Typical distributions of signal acceptance and efficiency as a function of the resonance pole mass are shown in Figure 4.1(left). The product of acceptance times efficiency is defined as the fraction of signal candidate events generated with a Born level dilepton mass greater than 60 GeV that pass full analysis selection requirements in the search region of $128 < m_{ll} < 4500$ GeV. For low values of the resonance masses, the distribution rises due to kinematic selection requirements. It drops again at high mass because of the strong decrease of the parton luminosity at high momentum transfer enhances relative fraction of events in the low-mass tail of the spectrum (*parton luminosity tail*) arising from the off-shell production as shown in the Figure 4.1(right).

[2] Paper is currently in preparation. The data are presented double differentially in invariant mass and absolute dilepton (pseudo-)rapidity.

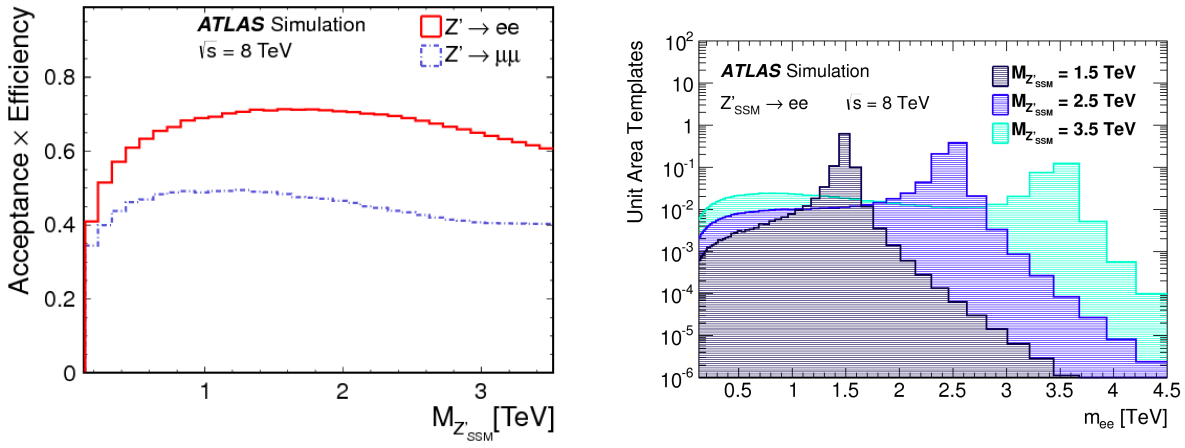

Figure 4.1: (left) Product of acceptance and efficiency as a function of the Z'_{SSM} pole mass. (right) Examples of dielectron signal templates at reconstruction level for the Z'_{SSM} signals.

4.2.3 Systematic Uncertainties

The treatment of systematic uncertainties in this analysis is simplified by the fact that the backgrounds are normalized to the data in the region of the Z peak. This removes all mass-independent uncertainties in this analysis as well as the luminosity uncertainty. A mass-independent error of 4% is assigned to the signal expectation due to the uncertainty on the Z/γ^* cross-section in the normalization region.

Mass-dependent systematic uncertainties include theoretical and experimental effects on the signal and background. They are correlated across all m_{ll} bins in the search region. The experimental uncertainties are fully correlated between the signal and all types of background. Details of systematic uncertainty calculation are given in Ref. [25]. Table 4.1 provides the typical values of uncertainties which change the expected number of events by at least 3% anywhere in the m_{ll} distribution. Uncertainties below this value have no impact on the analysis result and thus are neglected in the statistical analysis.

4.2.4 Comparison of data and background expectations

The observed dielectron and dimuon mass distributions after the full analysis selection are compared to the SM expectations. To make this comparison, the sum of all estimated backgrounds, with their relative contributions fixed according to their cross-sections is scaled such that the observed number agrees with the number of events in data in the $80 - 100\,\text{GeV}$ normalization region. The resulting scaling factor is 1.02 in the dielectron channel and 0.98 in the dimuon channel.

Figure 4.2 shows the m_{ll} distributions for the dilepton final states. Table 4.2 shows the number of data events and the estimated backgrounds in bins of reconstructed dielectron and dimuon invariant mass above 110 GeV. The dilepton invariant mass distributions are well described by the SM processes predictions.

Table 4.1: Summary of systematic uncertainties on the expected number of events at a dilepton mass of $m_{ll} = 3\,\text{TeV}$, where "n/a" indicates that the uncertainty is not applicable. Values are given in %.

Source	Dielectrons		Dimuons	
	Signal	Background	Signal	Background
Normalization	4	n/a	4	n/a
PDF variation	n/a	30	n/a	17
PDF choice	n/a	22	n/a	12
α_s	n/a	5	n/a	4
EW correction	n/a	4	n/a	3
PI correction	n/a	6	n/a	4
Beam energy	< 1	5	< 1	3
Resolution	< 3	< 3	< 3	8
Dijet and W+jets	n/a	21	n/a	n/a
Total	4	44	4	23

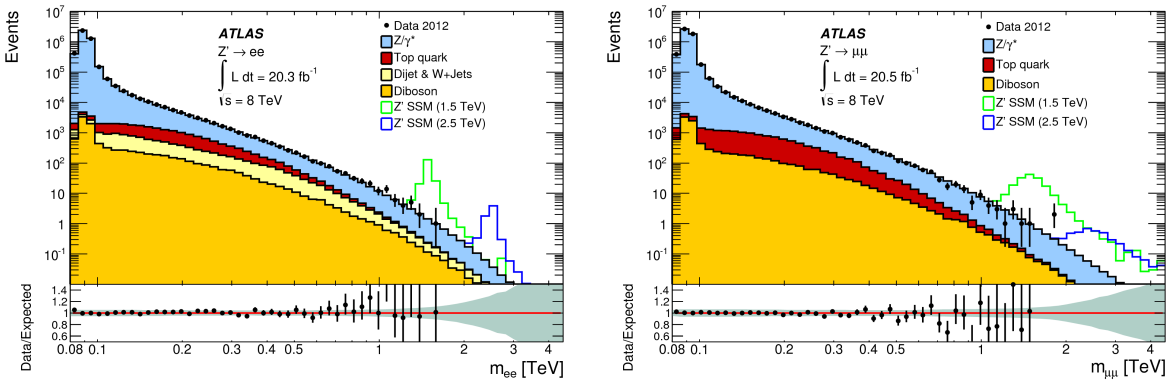

Figure 4.2: Invariant mass distribution for (left) dielectron and (right) dimuon events after the signal selection.

Table 4.2: The expected and observed number of events in the dielectron channel. The errors quoted include both statistical and systematic uncertainties.

m_{ee} [GeV]	110 - 200	200 - 400	400 - 800	800 - 1200	1200 - 3000	3000 - 4500
Z/γ^*	122000±7000	14000±800	1320±70	70±5	10.0±1.0	0.008±0.004
Top	8200±700	2900±500	200±80	3.1±0.8	0.16±0.08	<0.001
Diboson	1880±90	680±40	94±5	5.9±0.4	1.03±0.06	<0.001
Dijet, W+jet	3900±800	1290±320	230±70	9.0±2.3	0.9±0.5	0.002±0.004
Total	136000±7000	18800±1000	1850±120	88±5	12.1±1.1	0.011±0.005
Observed	136200	18986	1862	99	9	0

Table 4.3: The expected and observed number of events in the dimuon channel. The errors quoted include both statistical and systematic uncertainties.

$m_{\mu\mu}$[GeV]	110 - 200	200 - 400	400 - 800	800 - 1200	1200 - 3000	3000 - 4500
Z/γ^*	111000±8000	11000±1000	1000±100	49±5	7.3±1.1	0.034±0.022
Top	7100±600	2300±400	160±80	3.0±1.7	0.17±0.15	<0.001
Diboson	1530±180	520±130	64±16	4.2±2.1	0.69±0.30	0.0024±0.0019
Total	120000±8000	13700±1100	1180±130	56±6	8.2±1.2	0.036±0.023
Observed	120011	13479	1122	49	8	0

4.2.5 Results

The data distribution is compared to the background expectation in the full search range using a log-likelihood-ratio (LLR) test. The likelihood function is defined as the product of the Poisson probabilities over all mass bins in the search region

$$\mathcal{L} = \prod_{i}^{N_{bins}} \frac{e^{-n_i} n_i^{d_i}}{d_i!} G(\nu),$$

where the symbol n_i corresponds to expected number of signal and background events in bin i of the m_{ll} distribution, d_i is the observed number of events and $G(\nu)$ represents the Gaussian constraints for the set of nuisance parameters ν. When multiple channels are considered, the joint likelihood is the product of the individual likelihoods in each channel.

To assess the compatibility of experimental data with a specific signal hypothesis $H_{Z'}$, as compared to the null hypothesis H_0, a test is performed as a function of the Z' signal cross-section $\sigma_{Z'}$ and $m_{Z'}$. The LLR test-statistic is defined as:

$$\text{LLR} = -2ln\frac{\mathcal{L}(\text{data}|\sigma_{Z'}, M_{Z'}, \nu')}{\mathcal{L}(\text{data}|\sigma_0, \nu")},$$

where the numerator has signal present and denominator no signal, ν' and ν" represent best-value fit of the nuisance parameters for both cases. The global p-value in each channel is the probability, assuming no signal, of observing a value of LLR at least as consistent with the existence of the signal as the one observed in data, e.g. $p = p(\text{LLR} \leq \text{LLR}_{obs}|\text{H}_0)$. To obtain this value we follow the following procedure. Pseudo-experiments are used to obtain the LLR distribution in the $\sigma_{Z'}$ and $m_{Z'}$ plane. These distributions are summed starting from the observed LLR to the more negative values. To obtain the global p-value this sum is divided by the total number of the pseudo-experiments. The data are found to be consistent with the null hypothesis, with p-values of 27% in the dielectron channel and 28% in the dimuon channel, using templates for the Z'_{SSM} signal. Those values do not change significantly if other signal hypothesis are used.

In the absence of a signal, upper limits at 95% credibility level (CL) are set on the Z' production cross section times branching ratio to the dilepton final state (σB) using the same binned likelihood function as defined above in the framework of the the Bayesian Analysis Toolkit (BAT) [57]. A Markov Chain MC technique is used to integrate over the nuisance parameters. Uniform positive prior probability distribution is assumed for the parameters of interest.

The product of acceptance and efficiency for the signal as a function of mass is calculated separately for each channel and each signal hypothesis and propagated into the limits. The expected exclusion limits are determined as the median of the distribution of the limits from simulated pseudo-experiments. The combination of the dielectron and dimuon channels is performed under the assumption of lepton universality. For each systematic uncertainty correlation across the bins as well as between signal and background is accounted for.

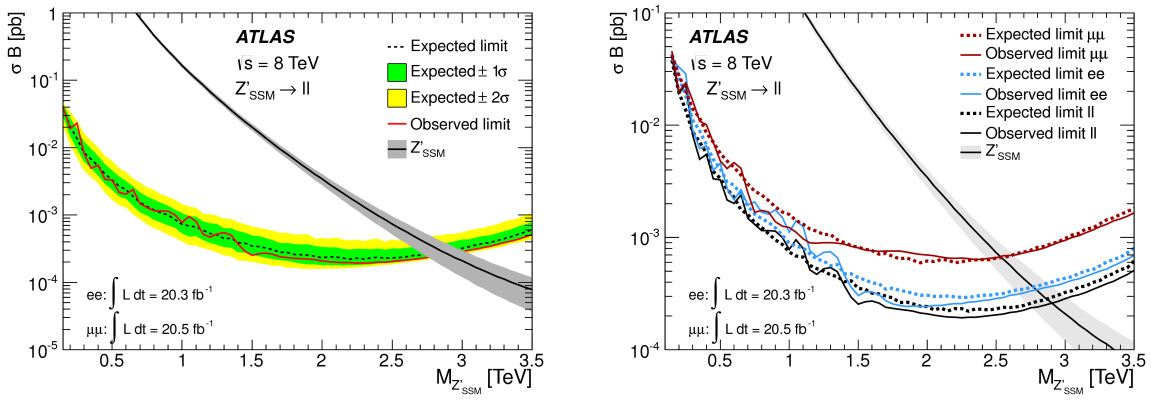

Figure 4.3: Median expected (dashed line) and observed (solid red line) 95% CL upper limits on cross-section times branching ratio (σB) in the combined dilepton channel (left) and dielectron and dimuon channels separately (right), along with predicted σB for Z'_{SSM} production. (left) The inner and outer bands show the range in which the limit is expected to lie in 68% and 95% of pseudo-experiments, respectively. The thickness of the Z'_{SSM} theory curve represents the theoretical uncertainty from the PDF error set and α_S, as well as the choice of PDF.

Upper limits on the σB for the Z'_{SSM} production and decay in the dielectron, dimuon and combined channels are shown in Figure 4.3. As expected electron limits are much better at high dilepton masses (above 1 TeV) due to higher electron reconstruction efficiency and resolution. The value at which the theory curve and the observed (expected) limit curve intersect corresponds to the observed (expected) mass limit at 95% CL. This value for the Z'_{SSM} boson in the combined dilepton channel is 2.90 TeV (2.87 TeV).

The results on the similar dataset from the CMS collaboration are shown in Figure 4.4. A Sequential Standard Model Z'_{SSM} resonance lighter than 2.90 TeV is excluded at 95% CL. One striking feature of the CMS cross-section ratio limit curve is that it is flat at high resonance masses, contrary to the ATLAS result shown in Figure 4.3(left).

To investigate the difference of the ATLAS and CMS cross-section limit line-shapes at high p_T I studied the limit behavior for a wider set of models.

One benchmark model frequently used in addition to the SSM is the E_6 grand unified symmetry model [44], where E_6 is broken into $SU(5)$ and two additional $U(1)$ groups, leading to new neutral gauge fields ψ and χ. The particles associated with the additional fields can mix to form a Z' state: $Z'(\theta_{E_6}) = Z'_{\psi}\cos(\theta_{E_6}) + Z'_{\chi}\sin(\theta_{E_6})$ (θ_{E_6} is the mixing angle between the two gauge bosons). The value of θ_{E_6} specifies the Z' boson coupling strength to SM fermions as well as its intrinsic width. The E_6 models predict narrower Z' signals than Z'_{SSM}. For example, Z'_{ψ} has a width of 0.5% of its mass, and Z'_{χ} has a width of 1.2% of its mass [58, 59].

Another interesting model to consider (at least from its signal-lineshape perspective) proposes

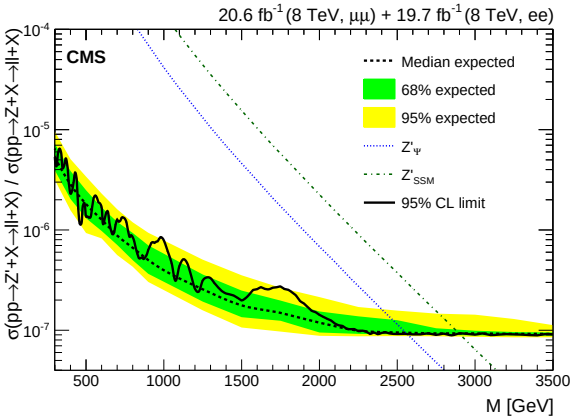

Figure 4.4: Upper limits as a function of the resonance mass M on the ratio of the product of cross section and branching fraction into lepton pairs relative to that of Z bosons, for final-state spins of 1. The shaded bands correspond to the 68% and 95% quantiles for the expected limits. Theoretical predictions for spin-1 resonances, Z'_{SSM} and Z'_{ψ} are shown for comparison. From Ref. [55].

Table 4.4: Observed and expected lower mass limits for Z' and Z^* bosons, using the corresponding signal template for a given model. Observed limits for the Z'_{SSM} model using all the other model templates are given in the last column.

Model	Width [%]	Observed Limit [TeV]	Expected limit [TeV]	Z'_{SSM} Expected Limit Equivalent [TeV]
Z'_{SSM}	3.0	2.90	2.87	2.90
Z'_{χ}	1.2	2.62	2.6	2.95
Z'_{ψ}	0.5	2.51	2.46	3.08
Z^*	3.4.	2.85	2.82	3.20

a solution to the SM hierarchy problem via the introduction of a new triplet of vector bosons: (Z^* and W^*) [60, 61]. To fix the Z^* boson coupling strength to fermions, a model with quark-lepton universality is adopted. The gauge coupling is chosen to be the same as in the SM $SU(2)$ group. The model parameters are chosen such that the total and partial decay widths of the W^* are the same for the W'_{SSM} (the charged partner of the Z'_{SSM}) at the same mass. The width of the Z^* resonance is 3.4% of its mass [60].

Summary of this study is presented in Figure 4.5 and Table 4.4 which show the observed upper limits at 95% CL on the σB for the various Z' model curves and a Z^* model. The main difference between three Z' resonances is their intrinsic width given in Table 4.4. Figure 4.5 shows that the limit values are strongly dependent on the width of the resonance in question, although the Z'_{SSM} limits remain conservative for the whole mass spectrum. At lower masses the resonances of the same width have the same limits, also the limits become stronger for the narrower resonances. At large resonance masses the limits for Z' models worsen with the increasing mass due to the presence of the parton-luminosity tail in the m_{ll} line-shape. The magnitude of this degradation is proportional to the size of the low-mass tail of the signal (which

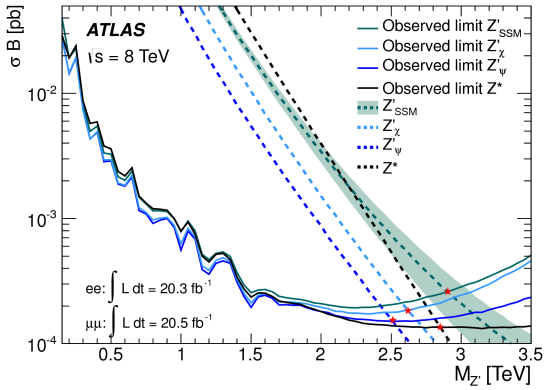

Figure 4.5: Observed upper cross-section times branching ratio limits at 95%CL for Z'_{SSM} E6-motivated Z' and Z^* bosons using the combined dilepton channel. Theoretical values for cross-section times branching ratio are shown for the same models. The stars indicate the lower mass limits for each considered model. The width of the Z'_{SSM} band represents the theoretical uncertainty from the PDF error set, the choice of PDF as well as the strong coupling constant. The width of this band applies to the E6-motivated Z' curves as well.

increases with the increase of the natural width of the Z' resonance). Limits for the Z^* model do not worsen with the increase in the invariant mass, because the tensor form of the coupling of the Z^* to fermions strongly suppresses parton luminosity effects.

Comparing Figure 4.4 and Figure 4.5 one can see that the Z^* limit shape is the most similar of the CMS result. This is due to the fact that CMS analysis uses signal shapes based on the convolution of a Breit-Wigner and a Gaussian resolution function [55], which does not have low-mass tail, just like the Z^* line-shape. To account for the difference between the full-shape and simplified model, in the CMS analysis [55] the calculated Z' cross sections include generated dileptons with masses only within ±5% of the nominal resonance mass. Otherwise as shown in the last column of Table 4.4, a simplified resonance line-shape such as a convolution of a Breit-Wigner and a Gaussian resolution would result in limits which are too aggressive if they are in the mass region close to the kinematic reach of the collider, where the parton-luminosity tail effects are significant.

In conclusion, the dilepton mass spectrum seen by the ATLAS experiment in the Run 1 LHC data is consistent with the SM expectation.

4.3 Combination of the neutral and charged leptonic decay channels of the new vector boson Run-1 searches

This work follows up on the ATLAS 8 TeV searches for new resonances in the high-mass dilepton [25] (Z') and lepton with $E_{\mathrm{T}}^{\mathrm{miss}}$ [62] (W') final states, in an attempt to find a new presentation of the ATLAS results which would simplify their reinterpretation into new not-yet-thought-of models. This work started in May 2014 as the corresponding publications were reaching completion and was done in collaboration with Manuel Perez-Victoria of the University of Granada.

In the cases where new resonances would result from extensions of the SM gauge group it is

possible to systematically classify them and parameterize in terms of mass and couplings. Gauge invariance under $SU(3)_C \times SU(2)_L \times U(1_Y)$ implies that there are only fifteen different multiplets of vector bosons which can be singly produced at colliders [63] (assuming renormalizable interactions to avoid suppressions from a higher scale). Of particular interest to the final states considered in this manuscript are singlets, such as Z' bosons associated with an extra $U(1)$ factors and isospin triplets which are formed by a neutral Z' boson and a pair of W' bosons. Experimentally, they are the only vector bosons that give rise to sizable resonant signals with leptonic final states at the LHC. They can also produce observable dijet and diboson signals.

It is common for the model-independent parameterizations in terms of couplings to use the narrow width approximation [58, 64]. Unfortunately the narrow width approximation does not work for bosons with mass close to the kinematic limit of the collider.

Our goal was to perform a complete general analysis for

- Singlet: six parameters, e.g. a mass and five couplings
- Triplet: four parameters, e.g. a mass, couplings to leptons (g_l) and quarks (g_q) and the Higgs field (g_ϕ).

For the singlet study, we investigated a possibility to reduce the six-parameter parameterization, but concluded that it is not possible to have a smaller set of parameters which would produce conservative limits in the full coupling-parameter space. We decided to upgrade the statistical framework of the dilepton search to accept the higher-dimensional template parameter-space. This task is still in progress.

The triplet study required a combination of the existing Z' and W' search results [25, 62]. We had to ensure that the analysis selections were orthogonal (e.g. had no events in common), to bring those analysis into the same statistical framework and to unify the systematic error treatment.

First we reviewed the analysis selections and we encountered the following issues:

- **Muon reconstruction.** The Z' muon reconstruction used Chain 1, while the W' used the Chain 2. Although the W' analysis required a veto on the second muon in the event, because muon reconstruction requirements were not identical the overlap in the Z' signal samples was $\sim$20% of the events.
- **Electron isolation** The W' analysis applied the same isolation criteria as the dielectron leading electron selection. The same isolation criteria were used to veto on the second electron in the event. But as described in Section 4.2.2 dilepton search in the electron channel used two different isolation selections for leading and subleading electrons, with the latter being a looser one. Even after the electron veto for the W' analysis, about 4% of the events in the Z' signal samples would pass both analysis selections.

Thus to proceed with the combination we would have to modify the W' selection as described above.

From the statistical interpretation point of view, the published W' search is basically a single-bin cut-and-count analysis. The Z' search uses templates in the full search range. To facilitate the combination we implemented the W' search (including full signal and background templates) in the BAT framework used by the dilepton team.

For the systematic error treatment, most of the uncertainties could be classified easily as either correlated and uncorrelated ones. This concerns uncertainties on the beam energy, electron

and muon reconstruction and identification, etc. Only one of the uncertainties caused a major problem, which was the show-stopper for this analysis. The PDF uncertainties for the W' search were implemented as a single parameter. The Z' analysis used a different approach. A single PDF error parameter led to over-constraint, while using all 20 PDF eigenvectors independently was prohibitive in terms of the computing time required by the statistical framework. Thus a set four eigenvector combinations with similar m_{ll} dependence was identified as described in Ref. [56] and used for the dilepton analysis. Unfortunately for the combination those PDF uncertainties are expected to be strongly correlated between the Z' and W' search channels but the study of those correlations had never been done before in this context.

When analysis reached this point, it was already May 2015 and 13 TeV data-taking was starting. At that point there was no available manpower to complete this major effort to reanalyze the old 8 TeV data. Thus the analysis team decided to postpone this combination effort to the Run-2 13 TeV data.

Both Z' and W' 13 TeV analyses have been performed coherently, taking into account the issues outlined above, which is expected to simplify the future combination.

4.4 My contributions

4.4.1 Convener of the Lepton+X group

I served as one of two conveners of the Lepton+X subgroup of the ATLAS Exotics Working group from 10/2012 to 09/2013. This group combines all analysis which have leptons and photons in the final state, e.g. dilepton, diphoton, lepton+$E_{\mathrm{T}}^{\mathrm{miss}}$, lepton+jet, lepton+jets, leptoquarks (all generations), excited leptons, multi-photons, lepton-flavor violating τ decays, lepton-flavor-violating Z' searches, etc. Overall this required coordination of work of over 100 physicists at various stages of their career. During this period the group has published four papers based on the 2011 data-set [65, 66, 67, 68] and one paper [69] and three conference notes based on the 2012 dataset [70, 71, 72].

4.4.2 Analysis contact responsible for combination of the neutral and charged decay channels of the new vector boson Run-1 searches

In May 2014 I was appointed as analysis contact responsible for generalization of the Run-1 dileptonic searches (which includes combination of the neutral and charged decay channels of the new vector boson Run-1 searches). Although this combination analysis was not completed, it produced recommendations for the Run-2 dilepton and lepton with $E_{\mathrm{T}}^{\mathrm{miss}}$ analyses, which have been implemented [73, 74] and which will facilitate combination of these channels in the future.

4.4.3 Contributions to the resonant search in dilepton channel

I supervised (2009-2012) Ludovica Aperio-Bella's thesis work [21] which contributed to Refs. [52, 53, 54]. I was also responsible for the Minimal-Walking-Technicolor MC simulation samples production, dielectron mass resolution studies, trigger strategy, etc.

For the Ref. [25], in 2012-2014, I was responsible for the full statistical analysis chain for the Minimal-Walking-Technicolor interpretation as well as the full set of the Z' templates in various models and their efficiency$\times$acceptance values.

I currently work with a post-doc, Paolo Mastrandrea, on electron performances at high-p_{T} for 13 TeV results at Run 2 [73].

4.4.4 Other responsibilities

I served as an Editorial Board chair or member for the internal review of three ATLAS papers [75, 76, 77] and six ATLAS conference notes [78, 79, 80, 81, 82] on searches in the ATLAS Higgs, SUSY and Exotic working groups which involve multilepton final states.

Chapter 5

Outlook

5.1 ATLAS detector upgrades for Run 3 and beyond

LHC 2016 data-taking is supposed to start shortly. After a rapid intensity ramp-up it should reach the nominal design luminosity of 10^{34} cm^{-2} s^{-1}. The expected integrated luminosity for 2016 is $25 - 30\,\text{fb}^{-1}$.

More extended LHC schedule is shown in Table 5.1. While the integrated luminosity accumulated by the LHC would be very beneficial to the physics analysis program, high luminosity values lead to high detector occupancy and high trigger rates.

During Run 3 the LHC luminosity could reach up to $3{\times}10^{34}$ cm^{-2} s^{-1}, twice higher than in Run 2, while the maximum possible ATLAS L1 rate is limited to 100 kHz. Following extensive discussions during LS1, it became clear that a further increase in the L1 trigger thresholds in particular for single electrons and muons is not desirable. Thus one has to find other means to achieve a factor of two or more background rejection at L1 for the Run 3. This approach requires upgrades to a few key sub-detectors prior to the start of that run.

One upgrade is the replacement of the inner stations of the endcap muon system with a new muon detector, the New Small Wheel [83], which provides additional coincidences to position and direction leading to a factor of two rate reduction for the L1 single muon trigger. The other is the upgrade of the LAr calorimeter electronics [20], which I am starting to work on.

As discussed earlier in sections 2.3.1 and 3.4.1 basic unit of the current L1Calo trigger is Trigger Tower that sums the energy deposition of sixty calorimeter cells in an area of $\Delta\eta \times \Delta\phi =$

Table 5.1: Expected evolution of the LHC settings with time. Note that the integrated luminosity values include the data-sets accumulated in the previous run periods. The higher peak luminosity value includes a margin taken by the ATLAS Collaboration for planning the detector upgrades.

Year	Energy [TeV]	Peak Luminosity [10^{34} cm^{-2} s^{-1}]	Integrated Luminosity [fb^{-1}]	Average pile-up
Design	14	1	-	25
2015-2018	13-14	1.6-2	100	43
2021-2024	14	2-3	300	50-80
2026-203x	14	5-7	3000	140-200

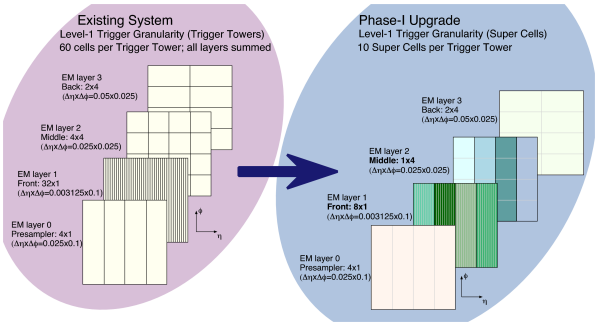

Figure 5.1: Geometrical representation in $(\eta \times \phi)$ space of an EM Trigger Tower in the current system, where the E_{T} in all four layers are summed (left) and of the Super Cells, where the transverse energy in each layer is retained in addition to the finer granularity in the front and middle layers (right). Each square represents an area of size $\Delta\eta \times \Delta\phi = 0.1 \times 0.1$. From Ref. [20].

0.1×0.1. To increase the L1Calo background rejection capabilities, in particular for the L1 electromagnetic triggers, one needs finer measurements of the shower development. A finer granularity scheme, called *Super Cells*, is proposed. In the footprint of the old Trigger Tower there will be one super cell in the pre-sampler, four in the front layer, four in the middle layer and one in the back layer as shown in Figure 5.1.

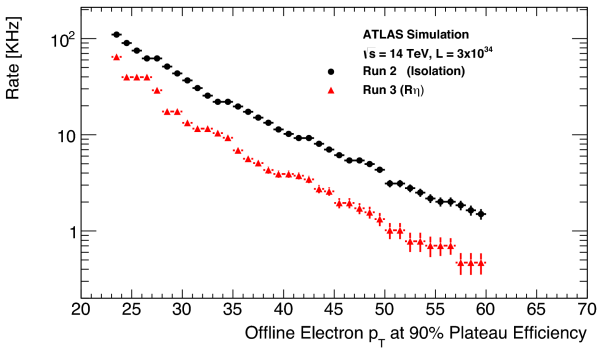

Figure 5.2: Rate improvement for a single EM cluster L1Calo trigger due to R_η selection in the Run 3 L1Calo system (triangle) compared to Run 2 (dot). From Ref. [26].

This order of magnitude increase in the granularity will allow the calculation in L1Calo of the basic shower shape variables, such as R_η which is the ratio of energy deposited in 0.075×0.2 region in $\eta \times \phi$ to a 0.175×0.2 region. An example of a typical rate improvement which would be achieved with this extra selection for a single electron trigger at L1 is shown in Figure 5.2.

In addition to the better discrimination against backgrounds and fakes, this upgrade improves the trigger energy resolution and efficiency for selecting calorimetric objects, such as electrons, photons, taus, jets, $E_{\mathrm{T}}^{\mathrm{miss}}$and $\sum E_T$.

To provide trigger signals with a higher spatial granularity to the L1Calo trigger, the LAr calorimeter read-out has to be modified. The architecture of the upgraded calorimeter electronics is depicted in Figure 5.3 with the upgraded and new components outlined in red.

New 124 LAr Trigger Digitizer Boards (LTDB), each handling up to 320 Super Cell channels, will be installed in the available spare slots of the Front-End crates. They will digitize the

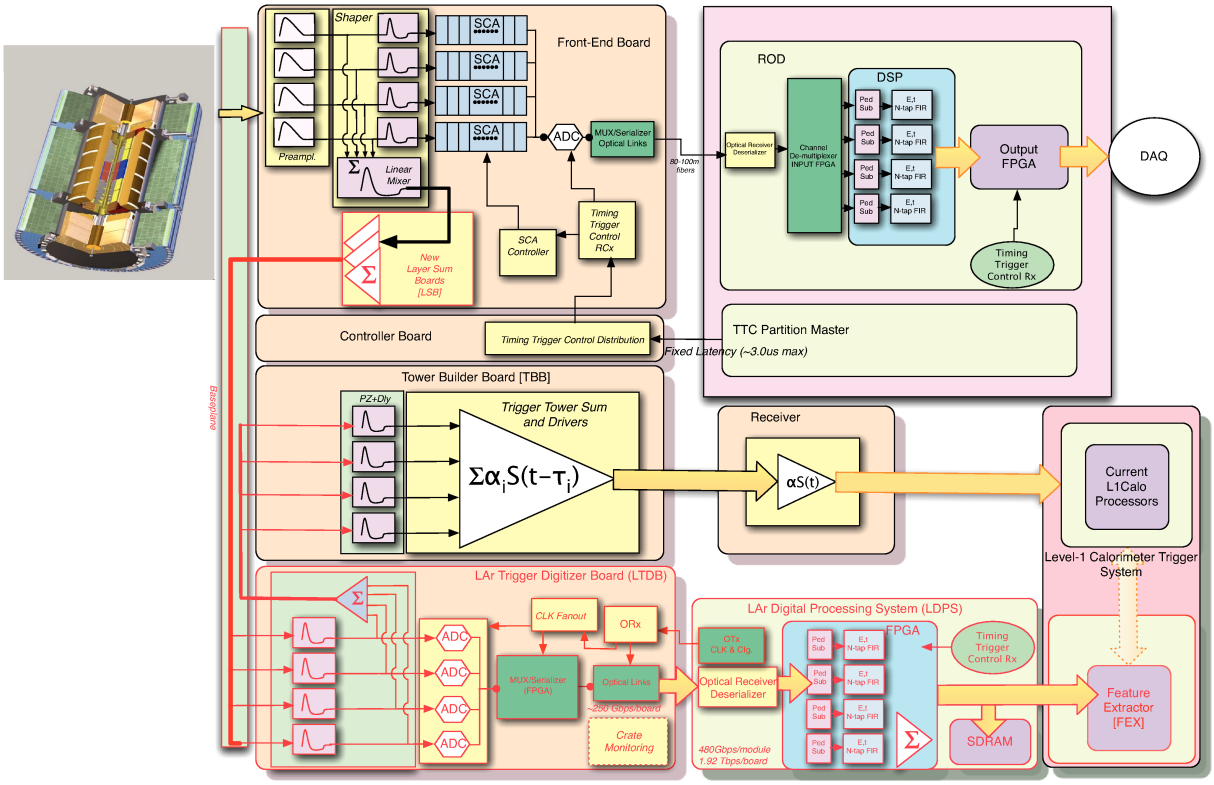

Figure 5.3: Schematic block diagram of the Phase-I upgrade LAr trigger readout architecture. The new components are indicated by the red outlines and arrows from Ref. [20].

detector pulses at 40 MHz and transmit the data to the back-end. The LTDB will also recreate the 0.1×0.1 analog sums and feed them back to the Tower Builder Board to maintain the legacy system fully operational for commissioning purposes.

The back-end system will receive the digitized data at a total rate of 25 Tb/s. The proposed system is made of 31 LAr Digital Processing Boards (LDPBs) housed in three ATCA (Advanced Telecom Computing Architecture) shelves. Each LDPB consists of one carrier board equipped with four LATOME (LAr Trigger prOcessing MEzzanine) cards. The design of the LATOME card (developed at LAPP) is built around one FPGA which will perform digital signal processing in real-time for precise energy reconstruction and bunch-crossing identification for up to 320 Super-Cells. These results are transmitted to the L1Calo in order to produce trigger decision.

In order to test the full functionality of the future LAr trigger system, a demonstrator setup has been installed on the ATLAS detector during LS1 and has been operating in parallel to the regular ATLAS data taking since early 2015. One Front-End Crate covering a region of one LAr half-barrel ($0.0 < \eta < 1.4$ and $9/16 \times \pi < \phi < 11/16 \times \pi$, i.e. about 2% of acceptance) is equipped with a prototype version of the system. The demonstrator allows to collect Run 2 data with Super Cells and do extensive validation of the firmware for energy reconstruction, bunch-crossing identification etc.

The first four prototype LATOME cards have been produced. They are currently undergoing various functionality tests to ensure that they work as intended.

In the next few years I will participate in the testing of the LATOME card, analysis of

the demonstrator data as well as firmware development (2016-2018). This will be followed by installation and commissioning of the complete system in-situ (2019-2021).

5.2 Perspectives for searches in the dilepton channel

The Run 1 of the LHC has seen major advances in particle physics, including the discovery of what is thought to be the last missing particle in the SM of the particle physics: a Higgs boson with a mass of around 125 GeV. One disappointing result of that run was the absence of new physics phenomena, with many mass limits reaching beyond a TeV [84, 85].

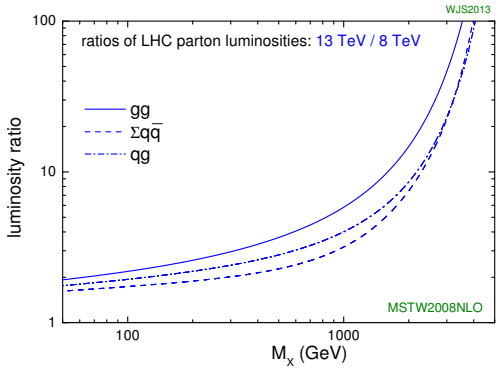

Figure 5.4: Expected parton luminosity increase due to the increase of the LHC center-of-mass energy from 8 TeV to 13 TeV. From [14].

The increase of the LHC center-of mass energy from 8 TeV in 2012 to 13 TeV in 2015 offered a unique opportunity to dramatically increase our sensitivity to the physics processes with high invariant masses due to a significant increase in the LHC parton luminosities shown in Figure 5.4. For example the cross-section increase for a Z' resonant state at 3 TeV is a factor of ten.

In 2015 the ATLAS experiment recorded 3.2 fb^{-1} of the LHC proton-proton collision data at $\sqrt{s} = 13$ TeV. Using dilepton invariant mass spectrum shown in Figure 5.5 as the discriminating variable limits on the Z'_{SSM} and Z'_{χ} mass limits were increased from 2.90 TeV and 2.62 TeV in 2012 [25] to 3.40 TeV and 3.08 TeV in 2015 [73]. Unfortunately there is still no sign of new phenomena in this channel.

On the other hand there are fascinating results in the corresponding dataset in the diphoton channel, shown in Figure 5.6. Both ATLAS and CMS experiments see an excess of events with a global significance of about 2 standard deviations around diphoton mass of 750 GeV [86, 87].

If the excess currently observed in the diphoton channel persists in the 2016 data, studying dielectron and dimuon decay channels would be critical to pin-point its nature. One of the typical benchmark models for a diphoton resonant search is a Kaluza-Klein excited graviton in Randall-Sundrum model (G^*) [45]. It has a universal coupling to all types of matter and gauge fields: $\sigma(pp \to G^* \to \gamma\gamma) = \sigma(pp \to G^* \to e^+e^- + \mu^+\mu^-)$ [88] thus is expected to result in a signal of a similar strength in dilepton channel while in most other models the dilepton final state is suppressed.

In the view of recent experimental results, for the 2016 dilepton analysis it is crucial to

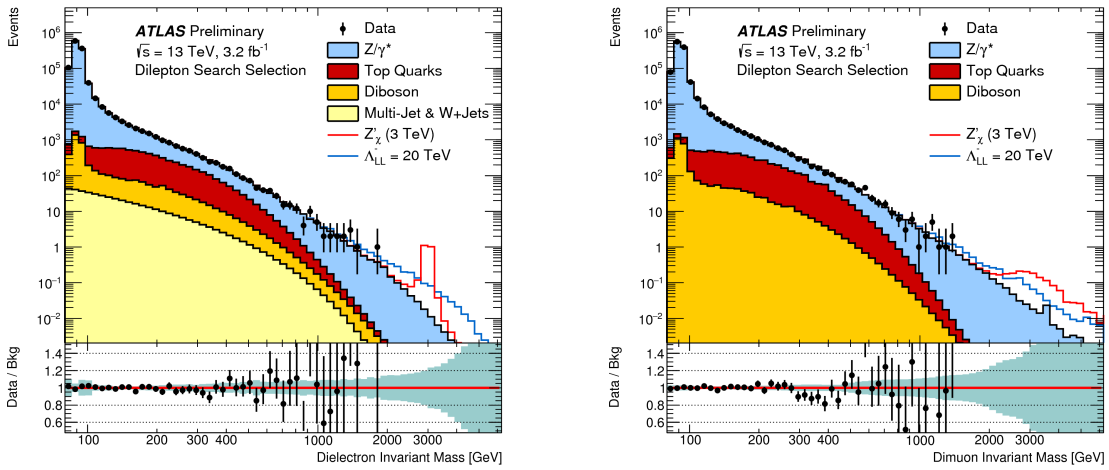

Figure 5.5: Invariant mass distribution of the selected (left) dielectron and (right) dimuon events for data and the SM background estimates as well as their ratio. From Ref. [73].

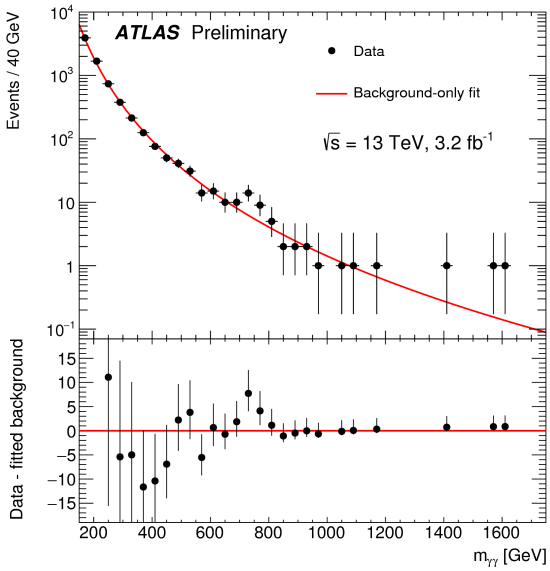

Figure 5.6: Invariant mass distribution of the selected diphoton events. Residual number of events with respect to the fit result is shown in the bottom pane. From Ref. [86].

implement a range of improvements, which would allow to maximize the analysis sensitivity, in particular for a mass around 750 GeV.

As discussed in the previous chapter, the dominant uncertainties in the dilepton analysis are theoretical in nature, and come from PDFs. Indeed, Z/γ^* production at invariant masses comparable to the beam energy requires both a quark and an antiquark with high momentum fraction x as shown in Figure 5.7. Because the PDFs of antiquarks are not well-known at such high x, the fractional uncertainty on the quark-antiquark luminosity becomes large, resulting in large uncertainties on the background and signal cross sections.

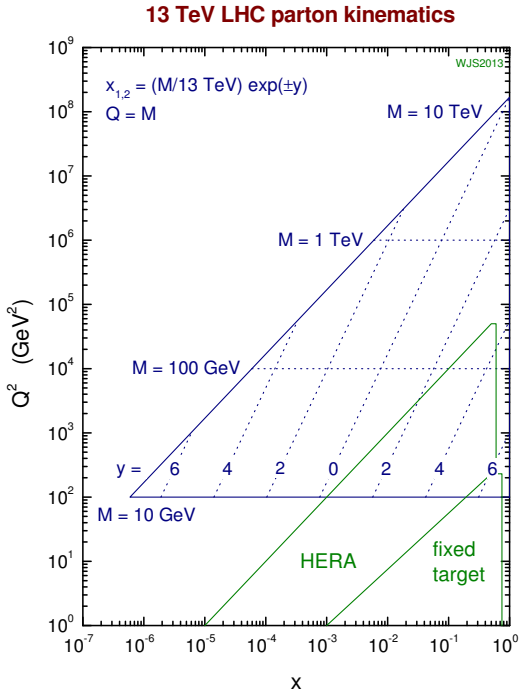

Figure 5.7: 13 TeV LHC parton kinematics from Ref. [14].

Measurement of the high-mass Drell-Yan differential cross-section at the LHC, similar to the one in Ref. [89] could help to constrain those uncertainties [90]. Using LHC data to improve background modeling potentially could remove or reduce non-resonant excesses, but it should not be a problem for the resonant ones. Note that the time-scale of this kind of analysis is very slow, e.g. only results from 7 TeV data-taking has been published up to date.

While the reduced PDF uncertainties are not available, there is an alternative approach in the lower dielectron mass region where the background is present in sufficient quantities. In this area we are able to model the background functional shape, fit it to data and to search for resonant structures on top of it. This would be an ideal approach for the 2016 data-taking and its implementation is on-going, led by the LAPP analysis team[1]. This method would have an additional advantage for the future analysis implementations as with ever-increasing dataset, it will be more and more difficult to produce MC simulation samples for background modeling in sufficient quantities, leading to higher uncertainty on the background predictions coming from the MC simulation statistics.

To further maximize the statistical significance of the discovery over the full search mass range it would also be possible to introduce electron categories in which events are classified according to the electron resolution as barrel-barrel, endcap-barrel or endcap-endcap.

[1]Dilepton analysis team at LAPP consists of two people a postdoc, Paolo Mastandrea and myself. There will maybe be a PhD students starting in November 2016.

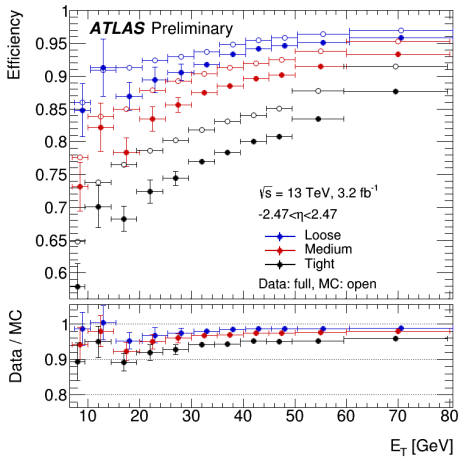

Figure 5.8: Electron identification efficiencies in $Z \to ee$ events as a function of E_{T} (from Ref. [91]).

We are also working on a better understanding of the electron performance at high-p_{T}. Using the non-resonant, Drell-Yan, events in addition to the resonant $Z \to ee$ decays should potentially allow to double the statistics of available electrons, allowing to extend the efficiency measurements in data to higher-p_{T} region than the current measurements shown in Figure 5.8 which go up to $\sim 80\,\mathrm{GeV}$. This work is also currently in progress.

As for the dilepton analysis potential at the high-mass-frontier: $25\,\mathrm{fb}^{-1}$ of data collected in 2016 will extend the range of dilepton discovery sensitivity to Z'-like final states up to 4 TeV. With $300(3000)\,\mathrm{fb}^{-1}$ the mass limit reach extends to 6.5(7.8) TeV-range [92].

With more data collected, in addition to pushing further the high-mass-frontier, we would be also sensitive to the lower cross-section signals, such as $H \to \mu\mu$, which could be observed at 2.3 (7.0) σ significance at $300(3000)\,\mathrm{fb}^{-1}$ respectively [93].

As discussed above, 2016 is a very important year for the dilepton analysis, and high-energy-physics in general and it is difficult to map-out the definite direction of the searches beyond it at this point.

5.3 Conclusions

The Standard Model is finally complete and there might be first hints of physics beyond Standard Model. LHC is still increasing its luminosity and maybe eventually the center-of-mass energy, which would allow us to follow up on any promising excesses quite quickly. ATLAS detector is ready to take data with well developed trigger menu strategy for the Run 2 and beyond. A whole suite of upgrades is in the pipe-line to enable us to use the LHC data to the full potential. Working on the ATLAS experiment has been an amazing adventure and will remain so for quite a few years to come. There is a lot of work ahead.

Bibliography

[1] E. D. Bloom et al., *High-Energy Inelastic e p Scattering at 6-Degrees and 10-Degrees*, Phys. Rev. Lett. **23** (1969) 930–934.

[2] M. Breidenbach et al., *Observed Behavior of Highly Inelastic Electron-Proton Scattering*, Phys. Rev. Lett. **23** (1969) 935–939.

[3] UA1 Collaboration, G. Arnison et al., *Experimental Observation of Isolated Large Transverse Energy Electrons with Associated Missing Energy at* $\sqrt{s} = 540\ GeV$, Phys. Lett. **B122** (1983) 103–116. [,611(1983)].

[4] UA2 Collaboration, M. Banner et al., *Observation of Single Isolated Electrons of High Transverse Momentum in Events with Missing Transverse Energy at the CERN anti-p p Collider*, Phys. Lett. **B122** (1983) 476–485.

[5] G. Arnison et al., *Experimental observation of lepton pairs of invariant mass around* $95\ GeV/c^2$ *at the CERN SPS collider*, Physics Letters B **126** no. 5, (1983) 398 – 410. http://www.sciencedirect.com/science/article/pii/0370269383901880.

[6] P. Bagnaia et al., *Evidence for* $Z^0 \to e^+e^-$ *at the CERN pp collider*, Physics Letters B **129** no. 1, (1983) 130 – 140. http://www.sciencedirect.com/science/article/pii/037026938390744X.

[7] CDF Collaboration, F. Abe et al., *Observation of top quark production in* $\bar{p}p$ *collisions*, Phys. Rev. Lett. **74** (1995) 2626–2631, arXiv:hep-ex/9503002 [hep-ex].

[8] D0 Collaboration, S. Abachi et al., *Search for high mass top quark production in* $p\bar{p}$ *collisions at* $\sqrt{s} = 1.8\ TeV$, Phys. Rev. Lett. **74** (1995) 2422–2426, arXiv:hep-ex/9411001 [hep-ex].

[9] DONUT Collaboration, K. Kodama et al., *Observation of tau neutrino interactions*, Phys. Lett. **B504** (2001) 218–224, arXiv:hep-ex/0012035 [hep-ex].

[10] ATLAS Collaboration, G. Aad et al., *Observation of a new particle in the search for the Standard Model Higgs boson with the ATLAS detector at the LHC*, Phys. Lett. **B716** (2013) 1–29, arXiv:1207.7214 [hep-ex].

[11] CMS Collaboration, S. Chatrchyan et al., *Observation of a new boson at a mass of 125 GeV with the CMS experiment at the LHC*, Phys. Lett. **B716** (2012) 30–61, arXiv:1207.7235 [hep-ex].

[12] M. Baak, J. Cúth, J. Haller, A. Hoecker, R. Kogler, K. Mönig, M. Schott, and J. Stelzer, *The global electroweak fit at NNLO and prospects for the LHC and ILC*, Eur. Phys. J. **C74** (2014) 3046, arXiv:1407.3792 [hep-ph].

[13] *Design Study of the LARGE HADRON COLLIDER*, Tech. Rep. CERN-91-03, CERN, Geneva, May, 1991.

[14] http://www.hep.ph.ic.ac.uk/~wstirlin/plots/plots.html.

[15] L. Evans and P. Bryant, *LHC Machine*, JINST **3** (2008) S08001.

[16] ATLAS Collaboration, G. Aad et al., *The ATLAS Experiment at the CERN Large Hadron Collider*, JINST **3** (2008) S08003.

[17] ATLAS Collaboration, G. Aad et al., *Electron performance measurements with the ATLAS detector using the 2010 LHC proton-proton collision data*, Eur. Phys. J. **C72** (2012) 1909, arXiv:1110.3174 [hep-ex].

[18] ATLAS Collaboration, G. Aad et al., *Electron and photon energy calibration with the ATLAS detector using LHC Run 1 data*, Eur. Phys. J. **C74** no. 10, (2014) 3071, arXiv:1407.5063 [hep-ex].

[19] ATLAS Collaboration, G. Aad et al., *Electron reconstruction and identification efficiency measurements with the ATLAS detector using the 2011 LHC proton-proton collision data*, Eur. Phys. J. **C74** no. 7, (2014) 2941, arXiv:1404.2240 [hep-ex].

[20] ATLAS Collaboration, *ATLAS Liquid Argon Calorimeter Phase-I Upgrade Technical Design Report* , Tech. Rep. ATLAS-TDR-22, CERN, Geneva, November, 2013.

[21] L. Aperio Bella, *Search for technihadrons in the dielectron mass spectrum and timing alignment of the ATLAS Liquid Argon Electromagnetic calorimeter*. Theses, Université de Grenoble, Sept., 2012. https://tel.archives-ouvertes.fr/tel-00744495.

[22] ATLAS Collaboration, G. Aad et al., *Monitoring and data quality assessment of the ATLAS liquid argon calorimeter*, JINST **9** (2014) P07024, arXiv:1405.3768 [hep-ex].

[23] ATLAS Collaboration, *Improved electron reconstruction in ATLAS using the Gaussian Sum Filter-based model for bremsstrahlung*, Tech. Rep. ATLAS-CONF-2012-047, CERN, Geneva, May, 2012. https://cds.cern.ch/record/1449796.

[24] ATLAS Collaboration, G. Aad et al., *Measurement of the muon reconstruction performance of the ATLAS detector using 2011 and 2012 LHC proton-proton collision data*, Eur. Phys. J. **C74** no. 11, (2014) 3130, arXiv:1407.3935 [hep-ex].

[25] ATLAS Collaboration, G. Aad et al., *Search for high-mass dilepton resonances in pp collisions at* $\sqrt{s} = 8$ *TeV with the ATLAS detector*, Phys. Rev. **D90** no. 5, (2014) 052005, arXiv:1405.4123 [hep-ex].

[26] ATLAS Collaboration, *TDR for the Phase-I Upgrade of the ATLAS TDAQ System*, Tech. Rep. ATLAS-TDR-23, CERN, Geneva, November, 2013.

[27] ATLAS Collaboration, *L1 Trigger Technical Design Report*, Tech. Rep. ATLAS-TDR-12, CERN, Geneva, Dec, 1998.

[28] ATLAS Collaboration, *ATLAS Detector and Physics Performance TDR*, Tech. Rep. ATLAS-TDR-14, CERN, Geneva, May, 1999.

[29] ATLAS Collaboration, G. Aad et al., *Performance of the ATLAS Trigger System in 2010*, Eur. Phys. J. **C72** (2012) 1849, arXiv:1110.1530 [hep-ex].

[30] ATLAS Collaboration, G. Aad et al., *Performance of the ATLAS muon trigger in pp collisions at* $\sqrt{s} = 8$ *TeV*, Eur. Phys. J. **C75** (2015) 120, arXiv:1408.3179 [hep-ex].

[31] https://twiki.cern.ch/twiki/bin/view/AtlasPublic/EgammaTriggerPublicResults.

[32] C. Doglioni, *Measurement of the Inclusive Jet Cross Section with the ATLAS Detector at the Large Hadron Collider*. Springer-Verlag Berlin Heidelberg, 2012.

[33] https://twiki.cern.ch/twiki/bin/view/AtlasPublic/TriggerOperationPublicResults.

[34] ATLAS Collaboration, G. Aad et al., *Triggers for displaced decays of long-lived neutral particles in the ATLAS detector*, JINST **8** (2013) P07015, arXiv:1305.2284 [hep-ex].

[35] Private communication with Frederik Ruehr.

[36] ATLAS Collaboration, G. Aad et al., *Search for new phenomena in the dijet mass distribution using* $p-p$ *collision data at* $\sqrt{s} = 8$ *TeV with the ATLAS detector*, Phys. Rev. **D91** no. 5, (2015) 052007, arXiv:1407.1376 [hep-ex].

[37] ATLAS Collaboration, G. Aad et al., *Performance of the ATLAS Trigger System in 2015*, in preparation (2016).

[38] T. Berger-Hryn'ova, *Study of B Meson Decays to p anti-p h Final States*. PhD thesis, SLAC, 2006. http://www-public.slac.stanford.edu/sciDoc/docMeta.aspx?slacPubNumber=slac-r-810.

[39] ATLAS Collaboration, G. Aad et al., *Expected Performance of the ATLAS Experiment - Detector, Trigger and Physics*, arXiv:0901.0512 [hep-ex].

[40] J. J. Aubert et al., *Experimental Observation of a Heavy Particle J*, Phys. Rev. Lett. **33** (1974) 1404–1406. http://link.aps.org/doi/10.1103/PhysRevLett.33.1404.

[41] J. E. Augustin et al., *Discovery of a Narrow Resonance in* e^+e^- *Annihilation*, Phys. Rev. Lett. **33** (1974) 1406–1408. http://link.aps.org/doi/10.1103/PhysRevLett.33.1406.

[42] S. W. Herb et al., *Observation of a Dimuon Resonance at 9.5 GeV in 400-GeV Proton-Nucleus Collisions*, Physical Review Letters **39** (1977) 252–255.

[43] P. Osland, A. A. Pankov, N. Paver, and A. V. Tsytrinov, *Sneutrino identification in dilepton events at the LHC*, Phys. Rev. **D82** (2010) 115017, arXiv:1008.1389 [hep-ph].

[44] P. Langacker, *The Physics of Heavy Z' Gauge Bosons*, Rev. Mod. Phys. **81** (2009) 1199–1228, arXiv:0801.1345 [hep-ph].

[45] L. Randall and R. Sundrum, *A Large mass hierarchy from a small extra dimension*, Phys. Rev. Lett. **83** (1999) 3370–3373, arXiv:hep-ph/9905221 [hep-ph].

[46] D0 Collaboration, V. M. Abazov et al., *Search for a heavy neutral gauge boson in the dielectron channel with 5.4 fb^{-1} of $p\bar{p}$ collisions at $\sqrt{s} = 1.96$ TeV*, Phys. Lett. **B695** (2011) 88–94, arXiv:1008.2023 [hep-ex].

[47] CDF Collaboration, T. Aaltonen et al., *Search for High Mass Resonances Decaying to Muon Pairs in $\sqrt{s} = 1.96$ TeV $p\bar{p}$ Collisions*, Phys. Rev. Lett. **106** (2011) 121801, arXiv:1101.4578 [hep-ex].

[48] OPAL Collaboration, G. Abbiendi et al., *Tests of the standard model and constraints on new physics from measurements of fermion pair production at 189-GeV to 209-GeV at LEP*, Eur. Phys. J. **C33** (2004) 173–212, arXiv:hep-ex/0309053 [hep-ex].

[49] DELPHI Collaboration, J. Abdallah et al., *Measurement and interpretation of fermion-pair production at LEP energies above the Z resonance*, Eur. Phys. J. **C45** (2006) 589–632, arXiv:hep-ex/0512012 [hep-ex].

[50] L3 Collaboration, P. Achard et al., *Measurement of hadron and lepton-pair production in e+ e- collisions at s**(1/2) = 192-GeV to 208-GeV at LEP*, Eur. Phys. J. **C47** (2006) 1–19, arXiv:hep-ex/0603022 [hep-ex].

[51] ALEPH Collaboration, S. Schael et al., *Fermion pair production in e^+e^- collisions at 189-209-GeV and constraints on physics beyond the standard model*, Eur. Phys. J. **C49** (2007) 411–437, arXiv:hep-ex/0609051 [hep-ex].

[52] ATLAS Collaboration, G. Aad et al., *Search for dilepton resonances in pp collisions at $\sqrt{s} = 7$ TeV with the ATLAS detector*, Phys. Rev. Lett. **107** (2011) 272002, arXiv:1108.1582 [hep-ex].

[53] ATLAS Collaboration, G. Aad et al., *Search for high mass dilepton resonances in pp collisions at $\sqrt{s} = 7$ TeV with the ATLAS experiment*, Phys. Lett. **B700** (2011) 163–180, arXiv:1103.6218 [hep-ex].

[54] ATLAS Collaboration, G. Aad et al., *Search for high-mass resonances decaying to dilepton final states in pp collisions at $\sqrt{s} = 7$ TeV with the ATLAS detector*, JHEP **11** (2012) 138, arXiv:1209.2535 [hep-ex].

[55] CMS Collaboration, V. Khachatryan et al., *Search for physics beyond the standard model in dilepton mass spectra in proton-proton collisions at $\sqrt{s} = 8$ TeV*, JHEP **04** (2015) 025, arXiv:1412.6302 [hep-ex].

[56] S. Viel, *Search for New Neutral High-Mass Resonances Decaying into Muon Pairs with the ATLAS Detector*. PhD thesis, TRIUMF, 2014. https://inspirehep.net/record/1339882/files/CERN-THESIS-2014-093.pdf.

[57] A. Caldwell, D. Kollar, and K. Kroninger, *BAT - The Bayesian analysis toolkit*, Computer Physics Communications **180** (2009) 2197–2209, arXiv:0808.2552 [physics.data-an].

[58] E. Accomando, A. Belyaev, L. Fedeli, S. F. King, and C. Shepherd-Themistocleous, *Z' physics with early LHC data*, Phys. Rev. D **83** (2011) 075012. http://link.aps.org/doi/10.1103/PhysRevD.83.075012.

[59] M. Dittmar, A.-S. Nicollerat, and A. Djouadi, *Z-prime studies at the LHC: An Update*, Phys. Lett. **B583** (2004) 111–120, arXiv:hep-ph/0307020 [hep-ph].

[60] M. V. Chizhov, *A Reference Model for Anomalously Interacting Bosons*, Phys. Part. Nucl. Lett. **8** (2011) 512–516, arXiv:1005.4287 [hep-ph].

[61] M. V. Chizhov, V. A. Bednyakov, and J. A. Budagov, *Anomalously interacting extra neutral bosons*, Nuovo Cim. **C033N5** (2010) 343–350, arXiv:1005.2728 [hep-ph].

[62] ATLAS Collaboration, G. Aad et al., *Search for new particles in events with one lepton and missing transverse momentum in pp collisions at $\sqrt{s}$ = 8 TeV with the ATLAS detector*, JHEP **09** (2014) 037, arXiv:1407.7494 [hep-ex].

[63] F. del Aguila, J. de Blas, and M. Perez-Victoria, *Electroweak Limits on General New Vector Bosons*, JHEP **09** (2010) 033, arXiv:1005.3998 [hep-ph].

[64] M. Carena, A. Daleo, B. A. Dobrescu, and T. M. P. Tait, *Z' gauge bosons at the Tevatron*, Phys. Rev. **D70** (2004) 093009, arXiv:hep-ph/0408098 [hep-ph].

[65] ATLAS Collaboration, G. Aad et al., *A search for high-mass resonances decaying to $\tau^+\tau^-$ in pp collisions at $\sqrt{s} = 7$ TeV with the ATLAS detector*, Phys. Lett. **B719** (2013) 242–260, arXiv:1210.6604 [hep-ex].

[66] ATLAS Collaboration, G. Aad et al., *Search for Extra Dimensions in diphoton events using proton-proton collisions recorded at $\sqrt{s} = 7$ TeV with the ATLAS detector at the LHC*, New J. Phys. **15** (2013) 043007, arXiv:1210.8389 [hep-ex].

[67] ATLAS Collaboration, G. Aad et al., *Search for contact interactions and large extra dimensions in dilepton events from pp collisions at $\sqrt{s} = 7$ TeV with the ATLAS detector*, Phys. Rev. **D87** no. 1, (2013) 015010, arXiv:1211.1150 [hep-ex].

[68] ATLAS Collaboration, G. Aad et al., *Search for third generation scalar leptoquarks in pp collisions at $\sqrt{s}$ = 7 TeV with the ATLAS detector*, JHEP **06** (2013) 033, arXiv:1303.0526 [hep-ex].

[69] ATLAS Collaboration, G. Aad et al., *Search for excited electrons and muons in $\sqrt{s}$=8 TeV proton-proton collisions with the ATLAS detector*, New J. Phys. **15** (2013) 093011, arXiv:1308.1364 [hep-ex].

[70] ATLAS Collaboration, *Search for excited electrons and muons with 13/fb of proton-proton collisions at $\sqrt{s} = 8$ TeV with the ATLAS detector* , Tech. Rep. ATLAS-CONF-2012-146, CERN, Geneva, November, 2012. https://atlas.web.cern.ch/Atlas/GROUPS/PHYSICS/CONFNOTES/ATLAS-CONF-2012-146.

[71] ATLAS Collaboration, *Search for high-mass dilepton resonances in 20/fb of pp collisions at $\sqrt{s} = 8$ TeV with the ATLAS experiment* , Tech. Rep. ATLAS-CONF-2013-017, CERN, Geneva, March, 2013. https://atlas.web.cern.ch/Atlas/GROUPS/PHYSICS/CONFNOTES/ATLAS-CONF-2013-017.

[72] ATLAS Collaboration, *A search for high-mass ditau resonances decaying in the fully hadronic final state in pp collisions at $\sqrt{s} = 8$ TeV with the ATLAS detector* , Tech. Rep. ATLAS-CONF-2013-066, CERN, Geneva, July, 2013. https://atlas.web.cern.ch/Atlas/GROUPS/PHYSICS/CONFNOTES/ATLAS-CONF-2013-066.

[73] ATLAS Collaboration, *Search for new phenomena in the dilepton final state using proton-proton collisions at $\sqrt{s} = 13$ TeV with the ATLAS detector*, Tech. Rep. ATLAS-CONF-2015-070, CERN, Geneva, December, 2015. https://atlas.web.cern.ch/Atlas/GROUPS/PHYSICS/CONFNOTES/ATLAS-CONF-2015-070.

[74] ATLAS Collaboration, *Search for new resonances in events with one lepton and missing transverse momentum in pp collisions at $\sqrt{s} = 13$ TeV with the ATLAS detector* , Tech. Rep. ATLAS-CONF-2015-063, CERN, Geneva, December, 2015. https://atlas.web.cern.ch/Atlas/GROUPS/PHYSICS/CONFNOTES/ATLAS-CONF-2015-063.

[75] ATLAS Collaboration, G. Aad et al., *Search for resonant WZ production in the $WZ \to \ell\nu\ell'\ell'$ channel in $\sqrt{s} = 7$ TeV pp collisions with the ATLAS detector*, Phys. Rev. **D85** (2012) 112012, arXiv:1204.1648 [hep-ex].

[76] ATLAS Collaboration, G. Aad et al., *Search for supersymmetry in events with three leptons and missing transverse momentum in $\sqrt{s} = 7$ TeV pp collisions with the ATLAS detector*, Phys. Rev. Lett. **108** (2012) 261804, arXiv:1204.5638 [hep-ex].

[77] ATLAS Collaboration, G. Aad et al., *Search for Higgs bosons decaying to aa in the $\mu\mu\tau\tau$ final state in pp collisions at $\sqrt{s} = 8$ TeV with the ATLAS experiment*, Phys. Rev. **D92** no. 5, (2015) 052002, arXiv:1505.01609 [hep-ex].

[78] ATLAS Collaboration, T. A. collaboration, *SUSY Searches at ATLAS in Multilepton Final States with Jets and Missing Transverse Energy*, tech. rep., 2011. https://atlas.web.cern.ch/Atlas/GROUPS/PHYSICS/CONFNOTES/ATLAS-CONF-2011-039.

[79] ATLAS Collaboration, T. A. collaboration, *Measurement of the ZZ production cross section in proton-proton collisions at 7 TeV with the ATLAS detector*, 2011. https://atlas.web.cern.ch/Atlas/GROUPS/PHYSICS/CONFNOTES/ATLAS-CONF-2011-107.

[80] ATLAS Collaboration, *Constraining the gauge-mediated Supersymmetry breaking model in final states with two leptons, jets and missing transverse momentum with the ATLAS experiment at $\sqrt{s} = 7$ TeV*, tech. rep., 2011. https://atlas.web.cern.ch/Atlas/GROUPS/PHYSICS/CONFNOTES/ATLAS-CONF-2011-156.

[81] ATLAS Collaboration, *Search for New Phenomena in Events with Three or more Charged Leptons*, tech. rep., 2011. https://atlas.web.cern.ch/Atlas/GROUPS/PHYSICS/CONFNOTES/ATLAS-CONF-2011-158.

[82] ATLAS Collaboration, *Search for supersymmetry in events with three leptons and missing transverse momentum in $\sqrt{s}$ =7 TeV pp collisions with the ATLAS detector*, tech. rep., 2012. https://atlas.web.cern.ch/Atlas/GROUPS/PHYSICS/CONFNOTES/ATLAS-CONF-2012-023.

[83] ATLAS Collaboration, *New Small Wheel Technical Design Report*, Tech. Rep. ATLAS-TDR-20, CERN, Geneva, June, 2013.

[84] https://twiki.cern.ch/twiki/bin/view/CMSPublic/PhysicsResultsEXO?rev=382.

[85] https://atlas.web.cern.ch/Atlas/GROUPS/PHYSICS/CombinedSummaryPlots/EXOTICS/.

[86] ATLAS Collaboration, *Search for resonances decaying to photon pairs in 3.2 fb^{-1} of pp collisions at $\sqrt{s} = 13$ TeV with the ATLAS detector* , Tech. Rep. ATLAS-CONF-2015-081, CERN, Geneva, December, 2015. https://atlas.web.cern.ch/Atlas/GROUPS/PHYSICS/CONFNOTES/ATLAS-CONF-2015-081.

[87] CMS Collaboration, *Search for new physics in high mass diphoton events in proton-proton collisions at $\sqrt{s} = 13$ TeV.* , Tech. Rep. CMS-PAS-EXO-15-004, CERN, Geneva, December, 2015.

[88] B. C. Allanach, K. Odagiri, M. J. Palmer, M. A. Parker, A. Sabetfakhri, and B. R. Webber, *Exploring small extra dimensions at the large hadron collider*, JHEP **12** (2002) 039, arXiv:hep-ph/0211205 [hep-ph].

[89] ATLAS Collaboration, G. Aad et al., *Measurement of the high-mass Drell–Yan differential cross-section in pp collisions at $\sqrt{s} = 7$ TeV with the ATLAS detector*, Phys. Lett. **B725** (2013) 223–242, arXiv:1305.4192 [hep-ex].

[90] J. Rojo et al., *The PDF4LHC report on PDFs and LHC data: Results from Run I and preparation for Run II*, J. Phys. **G42** (2015) 103103, arXiv:1507.00556 [hep-ph].

[91] ATLAS Collaboration, *Electron Efficiency Measurements in 2015 Data*, Tech. Rep. ATL-COM-PHYS-2015-1459, CERN, Geneva, December, 2015.

[92] *Studies of Sensitivity to New Dilepton and Ditop Resonances with an Upgraded ATLAS Detector at a High-Luminosity LHC*, Tech. Rep. ATL-PHYS-PUB-2013-003, CERN, Geneva, Feb, 2013. https://cds.cern.ch/record/1516108.

[93] *Projections for measurements of Higgs boson cross sections, branching ratios and coupling parameters with the ATLAS detector at a HL-LHC*, Tech. Rep. ATL-PHYS-PUB-2013-014, CERN, Geneva, Oct, 2013. https://cds.cern.ch/record/1611186.